MASARYKOVA UNIVERZITA
PŘÍRODOVĚDECKÁ FAKULTA
ÚSTAV TEORETICKÉ FYZIKY A ASTROFYZIKY

Bakalářská práce

MAGDALÉNA HŘIBOVÁ

Rozložení temné hmoty v galaxiích a galaktických kupách

Bakalářská práce

Magdaléna Hřibová

Bibliografický záznam

Autor: Magdaléna Hřibová
Přírodovědecká fakulta, Masarykova univerzita
Ústav teoretické fyziky a astrofyziky

Název práce: Rozložení temné hmoty v galaxiích a galaktických kupách

Studijní program: Fyzika

Studijní obor: Astrofyzika

Vedoucí práce: Mgr. Ing. arch. Petr Kurfürst, Ph.D.

Akademický rok: 2024/2025

Počet stran: XIV + 63

Klíčová slova: Temná hmota; Galaxie; Gravitační potenciál; Halo; Rotační křivka

Bibliographic Entry

Abstrakt

V současnosti se předpokládá, že vesmír je tvořen z 5 % baryonovou hmotou, z 26 % temnou hmotou a zbylých 69 % připadá na temnou energii. Bez existence temné hmoty by bylo velmi obtížné vysvětlit pozorované jevy, jako je například plochost rotačních křivek spirálních galaxií, příliš vysoká disperze rychlostí hvězd v eliptických galaxiích nebo přebytečná hmota, odhalená pomocí gravitačního čočkování. Přestože temnou hmotu již zvládáme detekovat, její složení stále zůstává záhadou.

V této bakalářské práci se věnujeme temné hmotě a tomu, jaké má své místo v galaxiích a galaktických kupách. V teoretické části rozebíráme, jaké známe typy galaxií a jakými zákony se galaxie řídí. Také se zde věnujeme povaze temné hmoty, jejímu možnému složení a důkazům její existence. V praktické části se zabýváme rotačními křivkami galaxií a dostáváme až k rozložení hustoty temné hmoty v těchto strukturách.

Abstract

The current assumption is, that the universe is composed of 5 % baryonic matter, 26 % dark matter and the remaining 69 % is dark energy. Without the existence of dark matter, it would be very difficult to explain observed phenomena, such as the flatness of the rotation curves of spiral galaxies, the excessively high values of velocity dispersion of stars in elliptical galaxies, as well as the abundance of mass revealed through gravitational lensing. Although we are already able to detect dark matter, its nature still remains a mystery.

This bachelor's thesis focuses on dark matter and its role in galaxies and galaxy clusters. In the theoretical part, we discuss the different types of galaxies and the laws that govern them. We also examine the essence of dark matter, its possible composition and the evidence for its existence. In the practical part, we focus on the analysis of rotation curves of galaxies, leading up to the determination of the distribution of dark-matter density within these structures.

MUNI
SCI

ZADÁNÍ
BAKALÁŘSKÉ PRÁCE

Akademický rok: 2024/2025

Ústav:	Ústav teoretické fyziky a astrofyziky
Studentka:	Magdaléna Hřibová
Program:	Fyzika
Specializace:	Astrofyzika

Ředitel *ústavu* PřF MU Vám ve smyslu Studijního a zkušebního řádu MU určuje bakalářskou práci s názvem:

Název práce:	Rozložení temné hmoty v galaxiích a galaktických kupách
Název práce anglicky:	Distribution of dark matter in galaxies and galaxy clusters
Jazyk práce:	angličtina

Oficiální zadání:

Rotation curves of galactic spirals or other luminous baryonic components are an accurate indicator of their gravitational potential. This procedure also estimates the celestial coordinates of the galaxy's kinematic center, its systemic velocity, degree of symmetry, and often its inclination angle. Such parameters and their profiles within the baryonic matter in galaxies and galaxy clusters of various luminosities and types is one of the main source of evidence for the existence of dark particles that govern the structure of the Universe. This bachelor thesis will contribute to study the complex scenario of the properties of dark halos of galaxies and galaxy clusters also in relation to the properties of the baryonic components they host.

Literatura:

Dark matter in the universe. Edited by John N. Bahcall - Tsvi Piran - Steven Weinberg. 2nd ed. London: World Scientific, 2004, xii, 233 p. ISBN 9812388419.

BINNEY, James a Scott TREMAINE. *Galactic dynamics*. 2nd ed. Princeton: Princeton University Press, 2008, xvi, 885. ISBN 9780691130279.

Vedoucí práce:	Mgr. Ing. arch. Petr Kurfürst, Ph.D.
Konzultant:	Mgr. Filip Hroch, Ph.D.
Datum zadání práce:	16. 5. 2024
V Brně dne:	24. 4. 2025

Zadání bylo schváleno prostřednictvím IS MU.

Magdaléna Hřibová, 17. 5. 2024
Mgr. Ing. arch. Petr Kurfürst, Ph.D., 9. 8. 2024
RNDr. Luboš Poláček, 4. 12. 2024

Poděkování

Na tomto místě bych chtěla poděkovat především vedoucímu mojí bakalářské práce Mgr. Ing. arch. Petru Kurfürstovi, Ph.D., za jeho čas, rady, pomoc a ochotu, které mně věnoval. Dále děkuji Prokopu Ohlídalovi, za pomoc s pořizováním fotografií galaxií k praktické části této práce. Také chci poděkovat všem svým blízkým, kteří mě podpořili, když to bylo potřeba.

Prohlášení

Prohlašuji, že jsem svou bakalářskou práci vypracovala samostatně pod vedením vedoucího práce s využitím informačních zdrojů, které jsou v práci citovány.

Brno 13. května 2025

. . . .
Magdaléna Hřibová

Contents

Introduction

The first hint of an unknown form of matter appeared in 1933, when Fritz Zwicky discovered a gravitational anomaly while studying the Coma Cluster. The mass calculated from the cluster's luminous components did not match the mass inferred from the observed velocities of its galaxies. This discrepancy suggested the presence of an invisible substance, now known as dark matter. Since then, extensive observational evidence has continued to support its existence. Further clues emerged in the 1970s, when Vera Rubin investigated the measurements of rotation curves of spiral galaxies, that have confirmed the necessity of dark matter halos (Rubin et al. 1978). Dark matter appears to be essential in all spiral galaxies, especially at large radii, where the rotation curves remain flat. This observed shape of the rotation curves is a sign of the hidden matter, which provides the necessary gravitational pull. Similar anomalies have been observed in elliptical galaxies, where the velocity dispersions of stars are way too high to be caused by just the luminous matter alone.

Today, dark matter is believed to be a non-baryonic form of matter that interacts only through gravity; however, its exact composition remains unknown. Several candidates have been proposed, including weakly interacting massive particles (WIMPs) and axions, but none have been directly detected so far.

This bachelor thesis aims to address the issue of dark matter in galaxies and galaxy clusters, with the practical part focusing on the rotation curves of spiral galaxies. By comparing observed rotation curves to those predicted by visible matter alone, we examined the need for a dark matter component. In addition to fitting observational data with theoretical halo models, we also employed a complementary approach based on Poisson's equation to derive the dark matter density profiles directly.

1.   Galaxies and Galaxy Clusters

1.1   Formation of Galaxies and Galaxy Clusters

According to our current understanding of galaxy formation, every galaxy develops within a dark-matter halo. The evolution and expansion of galaxies over time are closely linked to the growth of the halos that host them (Wechsler and Tinker 2018). Dark matter is thought to be the gravitational backbone on which galaxies and galaxy clusters form, shaping cosmic filaments of luminous structures.

As explained by Combes (2023), the dark-matter skeleton of the universe began to gravitationally collapse even before the recombination era, which occurred approximately 380 000 years after the Big Bang. That is the epoch when matter decoupled from radiation. Since dark matter does not interact with photons, it was not impeded by radiation pressure and could start forming gravitational potential wells or halos earlier than ordinary (baryonic) matter. Once baryons were no longer coupled to photons, they began to fall into these pre-existing dark-matter halos.

ESA's Euclid mission could be a key candidate to shed light on the mystery of dark matter. The **Euclid Dark Universe** mission was launched on July 1, 2023, and is expected to map the sky for over six years. The telescope is positioned at the Sun-Earth Lagrange Point 2 (L2) and is conducting two main surveys: the Euclid Wide Survey (EWS) and the Euclid Deep Survey (EDS). EWS covers about one-third of the sky (up to 14 500 deg^2) and obtains high-resolution images of a large number of galaxies and their distribution. EDS surveys a smaller area (around 50 deg^2) and is designed to detect even faint and distant galaxies. Euclid's observations will help to describe the structure of the universe known as the Cosmic Web (Fig. 1.2). On March 19, 2025, the first data release (Q1) from Euclid was announced (Euclid Consortium 2025a). Figure 1.1 shows some of the variously shaped galaxies observed by Euclid. This and further information can be found on the Euclid Consortium's website.
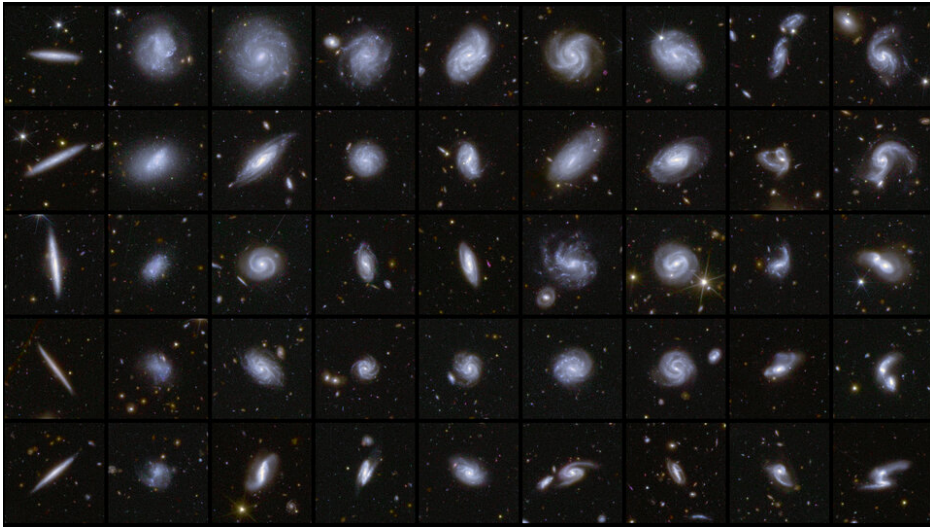
Figure 1.1: *Galaxies in different shapes captured by Euclid (ESA/Euclid/Euclid Consortium/-NASA et al. 2025).*
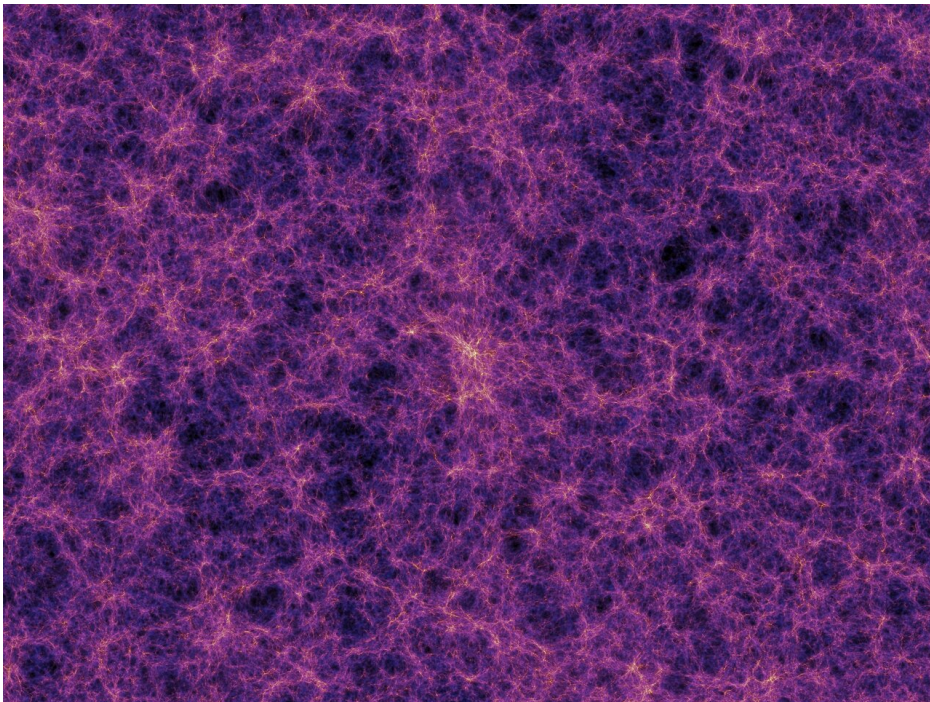
Figure 1.2: *The Cosmic Web (Artist's Impression) (Springel and Others 2020).*

Another mission that contributed to the dark-matter study is the **Hubble Space Tele-scope** (HST) through its survey, the **Cosmic Evolution Survey** ("COSMOS"). Using HST mapping, a three-dimensional map of the dark-matter distribution was created. This map helped confirm theories suggesting that galaxies form along clumps and fila-ments of dark matter, according to the ESA's website (ESA et al.) The top three images shown in Fig. 1.3 illustrate the evolution of dark-matter distribution over time. The bot-tom part of Fig. 1.3 presents a three-dimensional map of dark matter, constructed with respect to three axes: right ascension, declination, and distance from Earth (increasing from left to right). The picture shows that in the past, dark matter appeared to be more uniform.
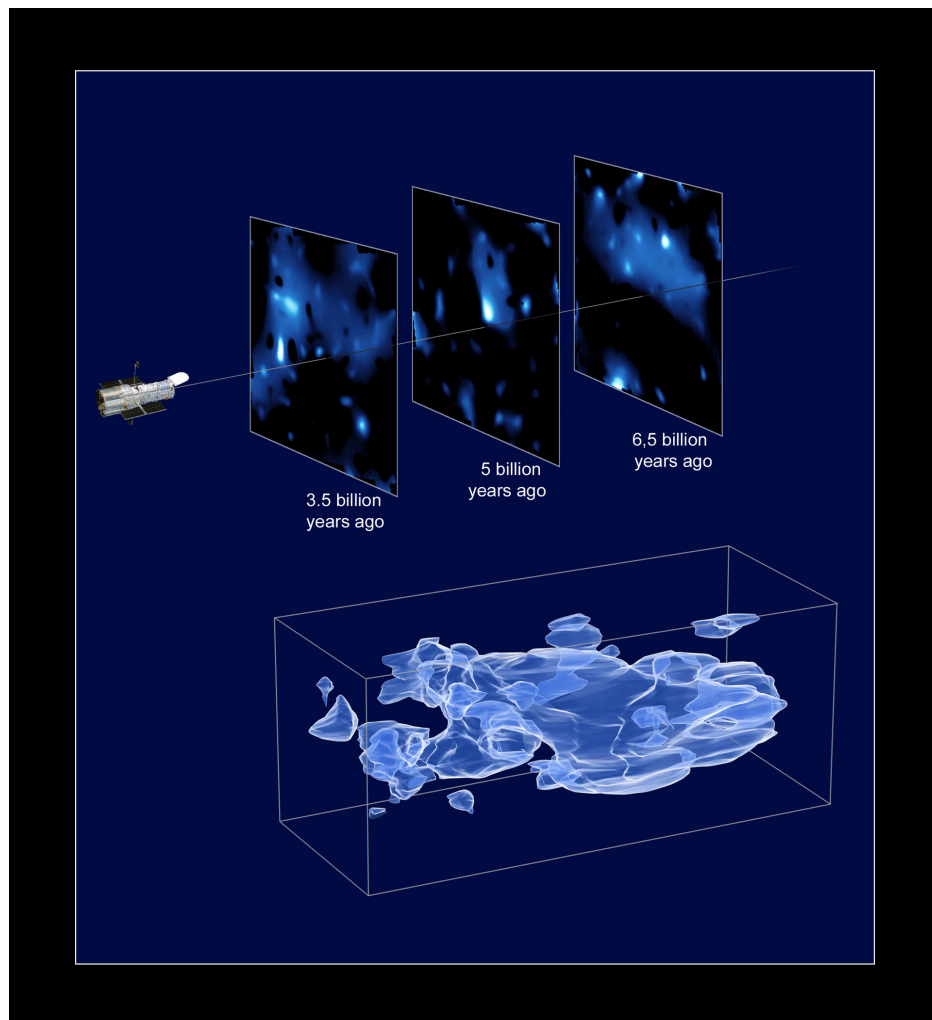
Figure 1.3: *3D map of dark matter as seen by Hubble (ESA et al. 2007).*

1.2 Types of Galaxies

There are many different shapes and sizes of galaxies. Based on these criteria, the Hubble classification, shown in Fig. 1.4, divides galaxies into three main types: spiral, elliptical, and lenticular. Irregular galaxies are those that could not be categorized as any of these three types. Originally, it was assumed that elliptical galaxies evolved into spiral galaxies. However, that was later discovered to be false (edited from Zejda (2013)).
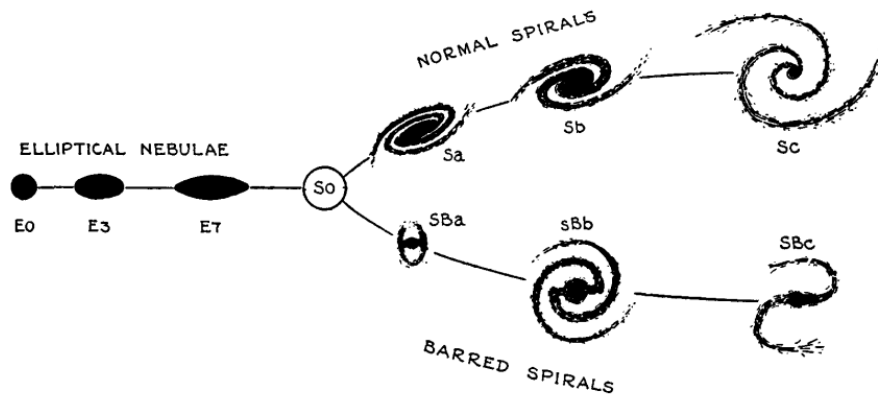
Figure 1.4: *The Hubble tuning fork - classification of galaxies (Hubble 1936).*

The original Hubble galaxy classification was improved by de Vaucouleurs (1963), who introduced a more elaborate categorization, especially for spiral galaxies. Figure 1.5 shows this refinement.
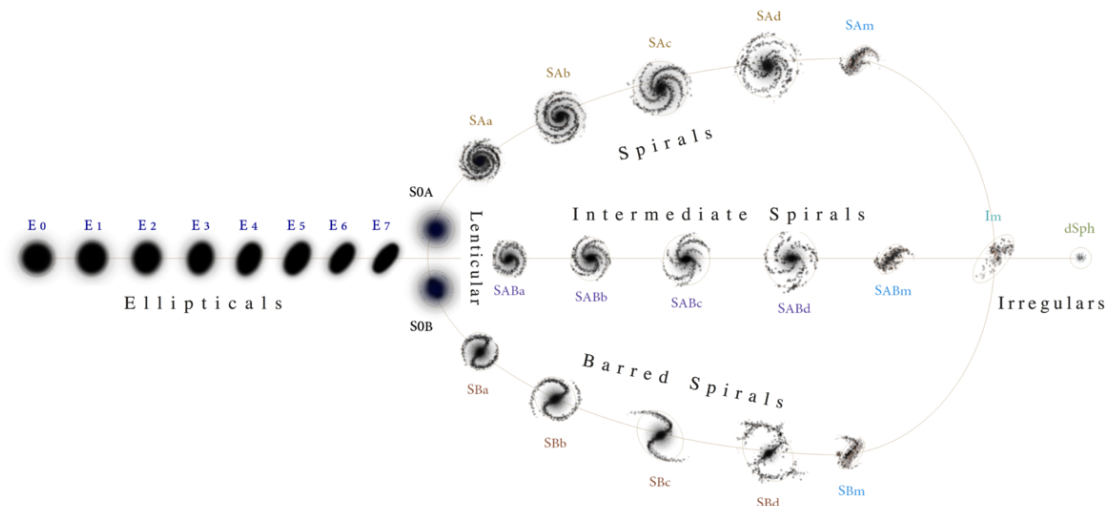
Figure 1.5: *The Hubble-de Vancoulers diagram (Ciccolella and De Leo 2016).*

Galaxies can also be classified according to their luminosity types, using a system proposed by van den Bergh (1960a,b,c). In this classification, galaxies are assigned a luminosity class ranging from *I* to *V*, where class *I* denotes the most luminous galaxies, and class *V* the least luminous. This classification is used in addition to the Hubble morphological types.

1.2.1 Elliptical Galaxies

Elliptical galaxies have the shape of a smooth sphere or a rotational ellipsoid. They contain mainly Population II stars, which are quite old, and little to no interstellar matter (dust and gas). That makes them poor in star-forming regions. These galaxies are denoted by symbols E0, E1, ..., E7, where the E0 galaxies are spherical and the E7 are the most elongated. The galaxies are labeled with numbers according to the formula Ex, where $x = 10[\frac{a-b}{a}]$, and a, b are the major and minor axes of the galaxy.

Most massive elliptical galaxies exhibit minimal or no rotation, even in cases where they have significantly elongated shapes. The stars within these galaxies move with random velocities along the line of sight, and the root mean square of this velocity dispersion can be determined from the Doppler broadening of their spectral lines (edited from Binney and Tremaine (1987)).

It was discovered by de Vaucouleurs (1948) that the surface brightness profile of elliptical galaxies approximately follows a decrease proportional to $r^{1/4}$. The so-called **de Vaucouleurs** profile is given by

$$I(r) = I_e \, 10^{-3.33([\frac{r}{r_e}]^{1/4}-1)}, \tag{1.1}$$

or equivalently, in its more commonly used form,

$$I(r) = I_e \, \mathrm{e}^{-7.67([\frac{r}{r_e}]^{1/4}-1)}, \tag{1.2}$$

where r_e is the effective radius (the radius within which half of the total luminosity of a galaxy is contained), and I_e is the surface brightness at r_e. As specified by Bovy (2023), the de Vaucouleurs profile does not describe smaller elliptical galaxies as well as it does the larger ones. For this reason, the **Sérsic** profile (Sersic 1968), which is a generalization of the de Vaucouleurs profile, is used as

$$I(r) = I_e \, \mathrm{e}^{-b_n([\frac{r}{r_e}]^{1/n}-1)}, \tag{1.3}$$

where b_n is given by $b_n = 2n - 0.324$ and n is a parameter that controls the shape of the profile (see Fig. 1.6).
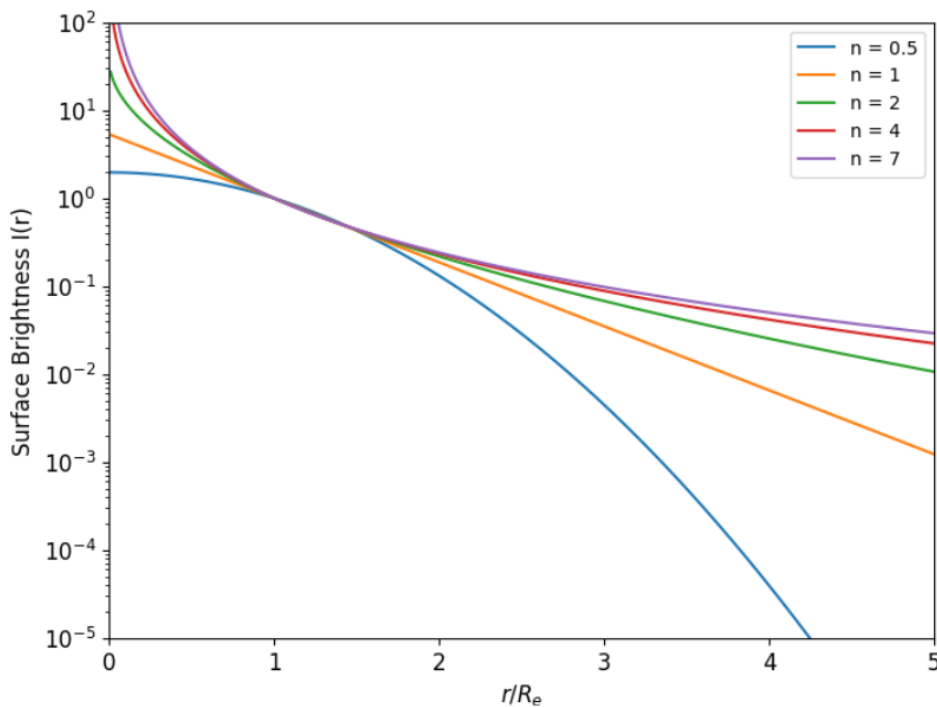
Figure 1.6: *Sérsic profiles for different values of n, with $r_e = 1$ and $I_e = 1$. The plot was generated using Equation* (1.3)*, implemented in NumPy and visualized with Matplotlib.*

1.2.2 Spiral Galaxies

Spiral galaxies consist of several distinct components, as Fig. 1.7 shows. Their prominent disks contain Population I stars, gas and dust. A defining feature of spiral galaxies is their spiral arms, which accommodate bright O and B stars and star-forming regions. The number and length of these arms can vary significantly from one galaxy to another. A central bulge contains older, Population II stars. The bulges of spiral galaxies exhibit diverse properties, reflecting different evolutionary processes. For example, as noted by Kormendy and Kennicutt (2004), classical bulges are typically formed through galaxy mergers and energetic interactions, whereas so-called pseudobulges form gradually from disk gas and retain features indicative of their disk origins. Although bulges have traditionally been compared to elliptical galaxies, recent observations indicate that some may share a closer connection with galactic disks (Moorthy and Holtzman 2006). At the center of spiral galaxies are supermassive black holes.

The Hubble-de Vaucouleurs classification of spiral galaxies divides them into these main types: Sa, Sb, Sc, Sd, and Sm. An "Sm" designation indicates a galaxy without a bulge and with an irregular structure. Sa-type galaxies have the highest luminosity in their stellar bulge and the most tightly wound spiral arms. When a spiral galaxy has a prominent bar, its designation includes a "B" (SBa, SBb, etc.). For weakly barred galaxies, "AB" is used in the notation, and for galaxies without bars, "A" is used. Additionally, the designations "r" and "s" are introduced, with "r" indicating a galaxy with a ring, "s" without a ring, and "rs" for intermediate cases (de Vaucouleurs 1963).

In most spiral galaxies, the circular velocity remains nearly constant across a wide range of radii. However, near the galactic center, the circular velocity decreases to zero. Typically, circular velocities outside the bulge are in the range of 200 to 300 km/s. A striking observation is that these velocity curves remain flat even at distances extending well beyond the visible boundaries of the galaxy, indicating the presence of an unseen or dark mass in its outer regions (edited from Binney and Tremaine (1987)). This flatness of rotation curves was discovered and studied by Vera Rubin. The radial surface-brightness profile of spiral galaxy disks can be described by the function

$$I(R) = I_0 \, e^{-\frac{R}{h_R}}, \tag{1.4}$$

where R is the radius and h_R is the scale length, according to Bovy (2023). From this function the galactic disks get their name - exponential disks.
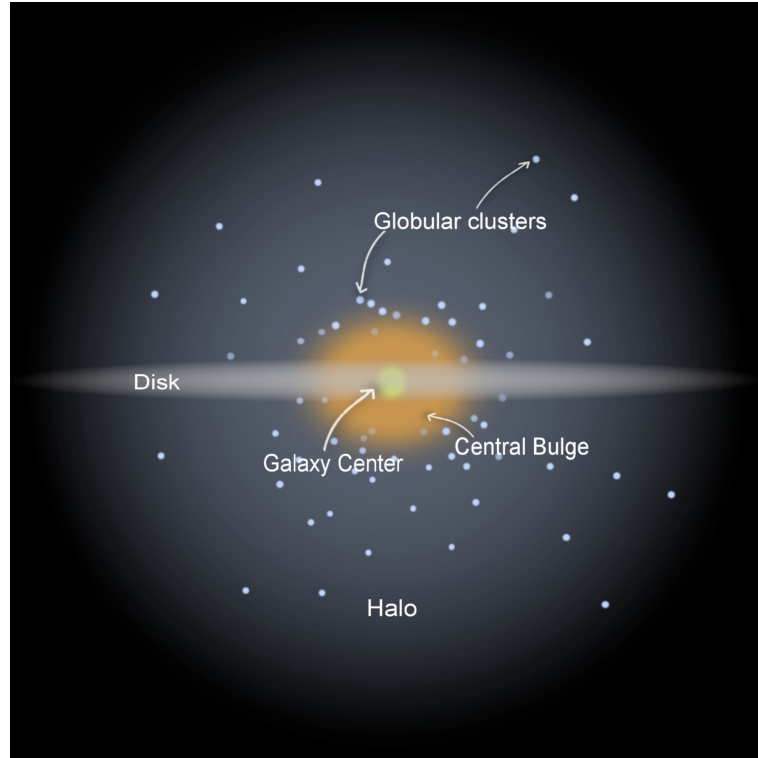
Figure 1.7: *Schematic picture of a spiral galaxy. Made using Picsart.*

By performing photometry of spiral galaxies, the radial surface brightness profile, $\mu(R)$, can be obtained. This profile can be decomposed into

$$\mu(R) = \mu_{\text{bulge}}(R) + \mu_{\text{disk}}(R). \tag{1.5}$$

Each component has its separate mass-to-light ratio, Y, defined as

$$Y = \frac{M}{L} = \frac{\text{Total mass}}{\text{Total luminosity}}. \tag{1.6}$$

The mass-to-light ratio is often expressed in solar units, where

$$Y_\odot = \frac{M_\odot}{L_\odot} = \frac{\text{Solar mass}}{\text{Solar luminosity}}. \tag{1.7}$$

Employing the mass-to-light ratios, the surface mass density $\Sigma(R)$ can be written as

$$\Sigma(R) = \Sigma_{\text{bulge}}(R) + \Sigma_{\text{disk}}(R) = Y_{\text{bulge}}\, \mu_{\text{bulge}}(R) + Y_{\text{disk}}\, \mu_{\text{disk}}(R). \tag{1.8}$$

1.2.3 Lenticular Galaxies

Lenticular galaxies, or S0 galaxies, according to the Hubble classification, represent an intermediate stage between elliptical and spiral galaxies, sharing features of both. They resemble spiral galaxies due to their prominent central bulge and disk, but are otherwise relatively featureless. Their disks lack spiral arms, gas, dust, and young stars. As specified by Binney and Tremaine (1987), these galaxies follow the surface-brightness law, that is given by Eq. (1.4).

1.3 Galaxy Clusters

Galaxy clusters are structures made up of a large number of galaxies, dark matter, and hot gas. They are the largest gravitationally bound objects in the universe. Assuming that the galaxy cluster is a closed system in a dynamical equilibrium, the virial theorem (see 2.5.1) can be applied, according to, e.g., Pfrommer (2022). The galaxies in a galaxy cluster - which may be about 10^3 galaxies for a rich galaxy cluster - have approximately a Gaussian velocity distribution and a velocity dispersion for such a rich cluster is $\sigma_v = \sqrt{\sigma_x^2 + \sigma_y^2 + \sigma_z^2} \approx 1200\,\text{km}\,\text{s}^{-1}$. By applying the virial theorem

$$2T + V = 0, \tag{1.9}$$

where T is the mean kinetic energy of the particles or bodies and V is their gravitational potential energy, we have

$$M_{\text{gal}}\, \sigma_v^2 - \frac{GM_{\text{cluster}}M_{\text{gal}}}{r_{\text{cluster}}} = 0, \tag{1.10}$$

where G is the gravitational constant. From Eq. (1.10), we can get the total mass of the cluster M_{cluster}. The typical radius r_{cl} is, as stated by Pfrommer (2022), $r_{\text{cl}} \approx 3\,\text{Mpc}$. From this

$$M_{\text{cluster}} = \frac{r_{\text{cl}}\sigma_v^2}{G} \approx 10^{15}\,\text{M}_\odot. \tag{1.11}$$

Even after adding up all the stellar masses of such a cluster, the obtained mass would still be insufficient compared to the reality ($M_{\text{stellar}} \approx \frac{1}{50} M_{\text{cl}}$ (Pfrommer 2022)). This discovery points to the existence of some unknown matter. However, to be more accurate, stars are not the only objects that add mass to the cluster. The space between the galaxies of a cluster is filled with hot gas, which emits X-ray radiation.

For the intracluster medium we can assume a hydrostatic equilibrium, since the gas is neither collapsing nor escaping the cluster. Therefore the inward and outward forces should be compensating as

$$E_{\text{thermal}} = V, \tag{1.12}$$

where E_{thermal} is the thermal energy of the gas particles equal to $\langle T \rangle$ and V is their potential energy. The hydrostatic balance

$$\frac{\partial P}{\partial r} = -\rho \frac{GM}{r^2}, \tag{1.13}$$

where $P(r)$ and $M(r)$ are the gas pressure and mass of the gas at some radius r, should be satisfied. The total thermal energy of an ideal gas, which we use as the overall assumption for the cluster's gas, is

$$E_{\text{thermal}} = \frac{3}{2} k_B \tau, \tag{1.14}$$

where τ is the temperature and k_B is the Boltzmann factor. For the gravitational potential energy of the gas particles, we will use the form

$$V = \mu \, m_p \frac{GM_{\text{cluster}}}{r_{\text{cluster}}}, \tag{1.15}$$

where μ is the mean molecular weight of primordial gas particles ($\mu \approx 0.588$ (Pfrommer 2022)). This value is used because the hot, fully ionized gas in galaxy clusters can be approximated as primordial gas (i.e., the composition resulting from Big Bang nucleosynthesis, consisting of roughly 76 % hydrogen and 24 % helium by mass) and m_p is the proton mass. As before, following Pfrommer (2022), the cluster mass can be acquired as

$$M_{\text{cluster}} = \frac{3 \, k_B \, \tau \, r_{\text{cluster}}}{2 \, \mu \, m_p \, G} \approx 2 \cdot 10^{48} \, \text{g} \approx 10^{15} \, \text{M}_\odot, \tag{1.16}$$

for a cluster with $k_B \tau = 6\,\text{keV}$. The gas mass obtained from the X-ray imaging of the cluster still appears to be much lower than the actual cluster mass, specifically $M_{\text{gas}} \approx \frac{1}{7} M_{\text{cluster}}$. The mass percentage of individual components is

$$M_{\text{stellar}} \approx 2\,\%,$$

$$M_{\text{gas}} \approx 13\,\%,$$

$$M_{\text{dark matter}} \approx 85\,\%.$$

One of the most significant proofs of dark matter is the **Bullet Cluster** (1E 0657-56), shown in Fig. 1.8. In the figure, the aftermath of a collision between two large galaxy clusters can be seen. As explained on the Chandra X-ray Observatory website, the pink regions represent the hot gas detected by **Chandra** in the X-ray spectrum, and it is clearly visible that the passage left a clump in the gas of one of the clusters. The gas

represents the largest amount of baryonic matter. The orange and white galaxies were captured by **Magellan** and **HST**. However, the highest concentration of mass is found in the blue areas, which were detected through the effects of gravitational lensing (see 2.6.2). The large mass density of these sections is attributed to dark matter. From the image, it can be concluded that the dark matter present in the clusters did not interact, unlike the gaseous parts.
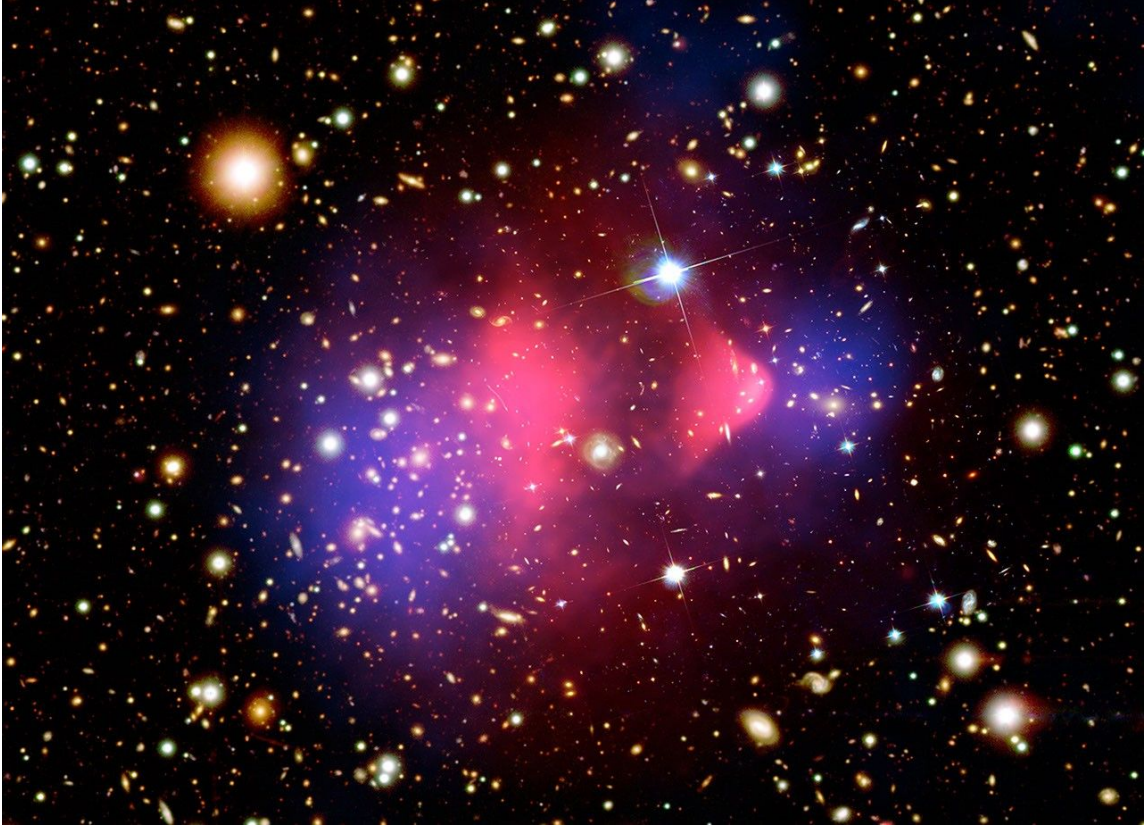
Figure 1.8: *Bullet Cluster (NASA/CXC/CfA/M. Markevitch et al. 2007).*

1.4   Galactic Dynamics

In this thesis, we use the notation R to denote the radial coordinate in cylindrical coordinates, and r for the radial coordinate in spherical coordinates.

1.4.1   Rotation Curves of Galaxies

The rotation curves of spiral galaxies reflect the dependence of the circular velocity v_c on the distance from the center r. Obtaining galactic rotational velocities is achieved through spectrometric measurements of stars or other luminous parts of galaxies, such as intragalactic gas. Objects moving away from us, the observers, exhibit a shift of their wavelengths toward the red end of the spectrum (redshift), while those moving closer

show a shift toward shorter wavelengths (blueshift). By measuring these shifts across different parts of a galaxy and accounting for its inclination, a rotation curve can be constructed.

In the inner regions of a galaxy, the rotation curve indicates that the galactic bulge behaves like a solid body, which means $v(r) \propto r$. As the curve reaches its peak, it transitions and exhibits a different dependence, which can be approximated by a constant v_c.

The rotation curve of a galactic disk reflects the mass distribution. Beyond a certain radius, the galaxy disk rotation curve remains approximately flat, which in the outermost regions is caused by the presence of a dark-matter halo (Sofue and Rubin 2001). The expected rotation curve behavior, in the absence of any unknown matter, is quite different. After reaching a peak - when the galactic bulge ends and the object can no longer be approximated as a solid body - the curve should follow the dependence $v(r) \propto 1/\sqrt{r}$. This discrepancy is attributed to the presence of dark matter, as mentioned earlier.

The **Tully–Fisher** law (Tully and Fisher 1977) is an empirically obtained relation, given by

$$L \propto v_{\text{rot, max}}^4, \tag{1.17}$$

under the assumption of a constant mass-to-light ratio Y and mean surface brightness, where L is the total luminosity and $v_{\text{rot, max}}$ is the maximum rotational velocity (Said 2023).

However, most observational studies have found that the power-law exponent deviates from the theoretical value, a discrepancy commonly attributed to the influence of dark-matter halos, as explained by Said (2023). To address this, the **baryonic Tully–Fisher relation** was proposed by McGaugh et al. (2000), which holds that

$$M_d \propto v_{\text{rot, max}}^4, \tag{1.18}$$

where M_d is the total baryonic mass, including both stars and gas $M_d = M_{\text{stellar}} + M_{\text{gas}}$.

1.4.2   Velocity Dispersion

Unlike in spiral galaxies, where the orbital motion of stars dominates, in elliptical galaxies, stars move in a more chaotic manner. To estimate the gravitational potential and the mass of elliptical galaxies, velocity dispersion is used. The velocity dispersion σ represents the statistical spread of velocities around the mean value for not only elliptical galaxies but also galaxy clusters.

The **Faber–Jackson** law (Faber and Jackson 1976) states that for elliptical galaxies, the total luminosity L is proportional to the fourth power of the central stellar velocity dispersion σ,

$$L \propto \sigma^4, \tag{1.19}$$

which is the analogy of Eq. (1.18) in the case of irregular or chaotic motion.

1.4.3   Description of Gravitation by Poisson's Equation

Poisson's equation is one of the fundamental equations of the theory of gravitation. It describes the relationship between the gravitational potential $\Phi(\mathbf{x})$ in a general coordi-

nate frame **x** and the spatial density distribution $\rho(\mathbf{x})$. This equation is given by

$$\Delta\Phi(\mathbf{x}) = 4\pi G\rho(\mathbf{x}), \tag{1.20}$$

where Δ is the Laplacian operator, and G is the gravitational constant.
Poisson's equation enables us to efficiently calculate gravitational potential (and, therefore, the spatial distribution of the gravitational acceleration) from an irregularly distributed matter or vice versa, usually using numerical or semi-analytical tools.

1.4.4 Gravitational Potential in Spherically Symmetric Matter Distribution

The gravitational potential Φ describes how the mass is distributed within a galaxy and determines the motion of objects within it. From the known density profile, in the case of spherical symmetry, where $\rho = \rho(r)$, the mass $M(r)$ contained within the radius r can be obtained by integrating

$$M(r) = 4\pi \int_0^r \rho(r')r'^2 dr'. \tag{1.21}$$

We can also obtain the gravitational potential $\Phi(r)$ at the radius r by integrating

$$\Phi(r) = -G \int_r^\infty \frac{M(r')}{r'^2} dr', \tag{1.22}$$

assuming zero gravitational potential at infinity.
For describing the distribution of dark matter in galaxy halos or elliptical galaxies, **the two-power density models** with density profile

$$\rho(r) = \frac{\rho_0\, a^\alpha}{r^\alpha \left(1 + \frac{r}{a}\right)^{\beta-\alpha}}, \tag{1.23}$$

where α and β are power indexes, ρ_0 is a scale density and a is the scale radius, are usually used. At the point where $r = a$ (the transition radius), ρ_0 is scaled by a numerical combination of α and β. From Eq. (1.23), we infer two density profiles,

$$\rho(r) = \rho_0 \left(\frac{a}{r}\right)^\alpha \quad \text{for} \quad r \ll a, \tag{1.24}$$

$$\rho(r) = \rho_0 \left(\frac{a}{r}\right)^\beta \quad \text{for} \quad r \gg a. \tag{1.25}$$

The most used variations of the two power density models are the **Navarro-Frenk-White (NFW) model**, introduced by Navarro et al. (1996), and the **Hernquist model**, derived by Hernquist (1990). The parameter values for NFW model are $\alpha = 1$, $\beta = 3$ and for the Hernquist model $\alpha = 1$, $\beta = 4$. We can obtain the mass $M(r)$ and potential $\Phi(r)$ for the NFW model, by following Eqs. (1.21) and (1.22). The resulting equations

describing the mass and gravitational potential profiles are

$$M(r)_{\mathrm{NFW}} = 4\,\pi\,\rho_0\,a^3\left[\ln\left(\frac{r}{a}+1\right)-\frac{r}{r+a}\right], \tag{1.26}$$

$$\Phi(r)_{\mathrm{NFW}} = -2\,\pi\,G\rho_0\,a^2\left[\frac{1}{r}\ln\left(\frac{r}{a}+1\right)\right]. \tag{1.27}$$

Similarly, the expressions for these quantities in the Hernquist model are given by

$$M(r)_{\mathrm{Hernquist}} = 2\,\pi\,\rho_0\,a^3\left(\frac{r}{r+a}\right)^2, \tag{1.28}$$

$$\Phi(r)_{\mathrm{Hernquist}} = -\frac{2\,\pi\,G\rho_0\,a^3}{r+a} = -\frac{G\,M_{r\to\infty}}{r+a}. \tag{1.29}$$

Apart from these models, dark-matter halos are also well approximated by an isothermal sphere, for which the density is given by

$$\rho(r)_{\mathrm{iso}} = \rho_0\left[1+\left(\frac{r}{r_c}\right)^2\right]^{-1}, \tag{1.30}$$

where ρ_0 is the central halo density and r_c is the halo core radius (Begeman et al. 1991).

1.4.5   Gravitational Potential in Disk-Like Structures

The gravitational potential of the galactic disk gives a connection between quantities such as the orbital velocity v_ϕ and the mass distribution, that can be described by the surface density $\Sigma(R,\phi)$ or the volume density $\rho(R,\phi,z)$. Assuming circular orbits, $v_\phi = v_{\mathrm{circ}}$, through the vertical range of the disk ($\mathrm{d}\Phi/\mathrm{d}z = 0$), then the circular velocity can be expressed from the definition of centripetal acceleration

$$a_R = -\frac{v_{\mathrm{circ}}^2}{R} \tag{1.31}$$

as

$$v_{\mathrm{circ}}^2 = R\frac{\mathrm{d}\Phi}{\mathrm{d}R}, \tag{1.32}$$

where the centripetal acceleration is identified as the gravitational acceleration

$$a_R = -\frac{\mathrm{d}\Phi}{\mathrm{d}R}. \tag{1.33}$$

Disk-like structures, for example a spiral galaxy, can be approximated as axially symmetric, where $\frac{\partial\Phi(R,\phi,z)}{\partial\phi} = 0$. This approximation overlooks the fact that some disk galaxies have spiral structure or bars (Bovy 2023).

For an axisymmetric, zero thickness (razor-thin) disk, the density takes the form

$$\rho(R,\phi,z) = \Sigma(R)\delta(z), \tag{1.34}$$

where $\delta(z)$ is the Dirac delta function. Following Poisson's equation (1.20), the general form for the gravitational potential for this type of disk is

$$\left.\frac{\partial \Phi(R,z)}{\partial z}\right|_{z=0} = 2\pi G \Sigma(R). \tag{1.35}$$

The potential used to describe a razor-thin disk may be, for example, expressed as

$$\Phi(R,z) = -\frac{GM}{\sqrt{R^2 + (|z| + a)^2}}, \tag{1.36}$$

which is called the **Kuzmin** model, where $a \geq 0$ is a scaling parameter of the model. As described by Bovy (2023), for $z > 0$, this potential is similar to the point-mass potential, which is given by

$$\Phi(R,z) = -\frac{GM}{\sqrt{R^2 + z^2}}. \tag{1.37}$$

One of the potentials that can be used to describe a disk with finite thickness is the **Miyamoto-Nagai** potential. This potential is given by the equation

$$\Phi(R,z) = -\frac{GM}{\sqrt{R^2 + (\sqrt{z^2 + b^2} + a)^2}}, \tag{1.38}$$

where M is the total mass of the disk, a is the horizontal scale length (disk scale radius), b is the vertical scale height of the disk, G is the gravitational constant, and R and z are galactocentric coordinates (Miyamoto and Nagai 1975) within a given galaxy. The profiles of the two potentials with the selected ratios of the parameters are compared in Fig. 1.9.
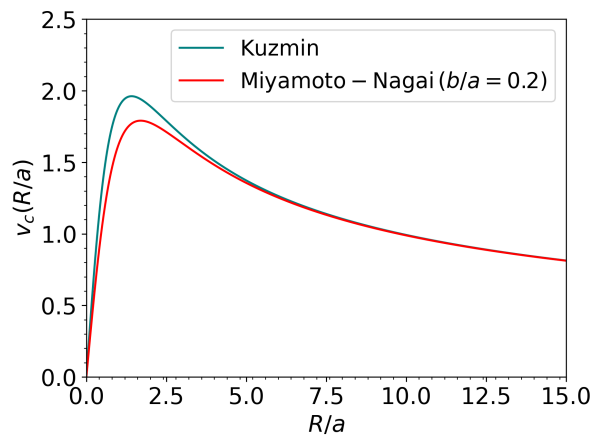
Figure 1.9: *An example of Kuzmin versus Miyamoto-Nagai potential (made using Galpy package (Bovy 2015)).*

2.   Dark Matter

According to the standard model of cosmology (Λ**CDM**), the universe consists of approximately 5 % baryonic matter, 26 % cold dark matter, and 69 % dark energy (Planck Collaboration and Others 2016). The so-called Hubble constant, H_0, is a parameter that describes the expansion rate of the universe. It is defined as

$$H_0 = \frac{\dot{r}}{r},\tag{2.1}$$

where r is the distance between two objects and $\dot{r}$ is the time derivative of that distance, i.e., the expansion velocity (Mikulášek and Krtička 2005). According to Planck Collaboration and Others (2016), the value of this parameter measured by the **Planck** space telescope is $H_0 = (67.8 \pm 0.9)\,\mathrm{km\,s^{-1}Mpc^{-1}}$.

2.1   Cosmic Microwave Background

There have been three major missions dedicated to observing the Cosmic Microwave Background (CMB). With the advancement of instrumentation, progressively more detailed CMB maps have been produced, as you can see in Fig. 2.1.
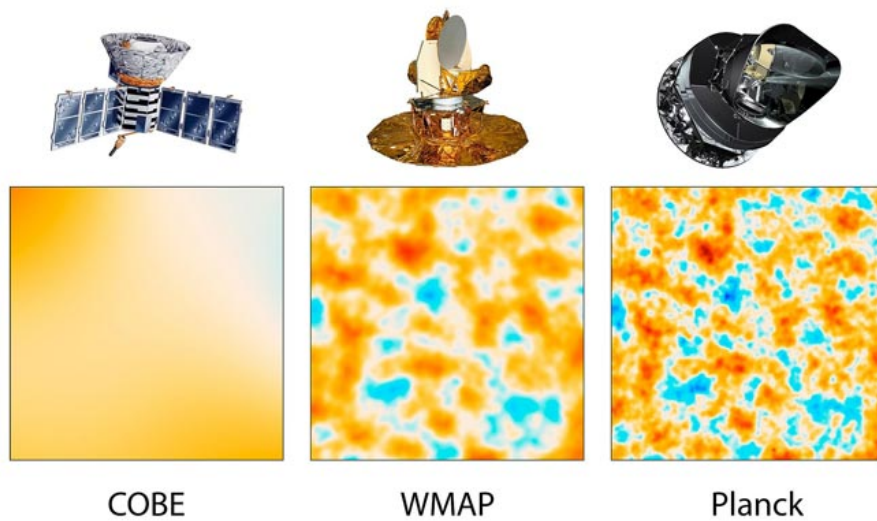
Figure 2.1: *The evolution of satellites designed to measure CMB (NASA et al. 2013).*

As explained by Freese (2017), analysis of the CMB reveals, as previously mentioned, that approximately 5% of the universe consists of ordinary (baryonic) matter, while about 26% is composed of dark matter.

2.2 The Shape of the Universe

Determining the geometry of the universe is crucial for understanding its ultimate fate. Will it collapse or will it continue expanding forever, eventually leading to a state of heat death? There are three possible types of curvature for the universe: flat, open, or closed (Kamionkowski 1998). The geometry of the universe is determined by its density. The critical density — the density the universe must have in order to be spatially flat — is given by

$$\rho_c = \frac{3\,H_0^2}{8\,\pi\,G},\tag{2.2}$$

where H_0 is the Hubble parameter and G is the gravitational constant. The density parameter Ω, which is also used, is defined as

$$\Omega = \frac{\rho}{\rho_c},\tag{2.3}$$

where ρ is the observed density of the universe. Figure 2.2 illustrates that the shape of the universe depends on the value of Ω. If $\Omega = 1$, the universe is flat and follows the rules of Euclidean geometry. If $\Omega < 1$, the universe is open and has a negative (saddle-shaped) curvature. For $\Omega > 1$, the universe is closed and has a positive (spherical) curvature.

Figure 2.2: *Geometry of the universe (NASA and WMAP Science Team (2011)).*

It is currently believed that the universe is flat. According to Lahav and Liddle (2004), the total matter density Ω_m is

$$\Omega_m = \Omega_c + \Omega_b,\tag{2.4}$$

where Ω_b represents the matter associated with baryons and Ω_c is the cold dark-matter density. Cold dark matter is one of the most widely supported predictions about the nature of dark matter, despite its shortcomings on smaller scales (such 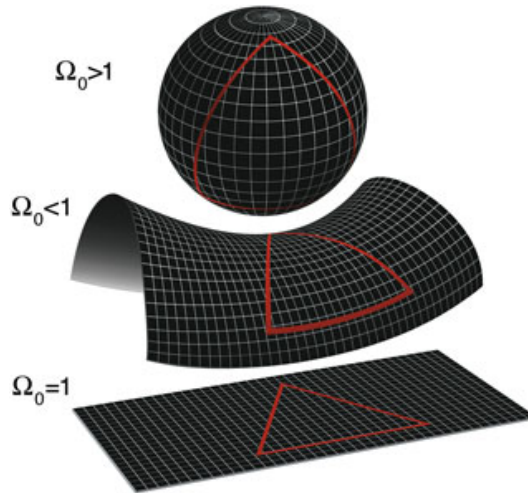as in dwarf galaxies). Another, though less recognized, type is hot dark matter, which prevents galaxy formation due to its higher velocity. Although the cold dark matter is currently the most commonly supported theory, it is still possible that dark matter exists as a combination of these two components (Lahav and Liddle 2004).

In keeping with the same article, two studies - the *Supernova Cosmology Project* and the *High-z Supernova Search Team* - concluded that the dark energy component (cosmological constant Λ) causes the universe to accelerate. The CMB data implies that the universe is flat ($\Omega_m + \Omega_\Lambda = 1$) and it is estimated, as already suggested, that the values $\Omega_m \approx 0.3$ and $\Omega_\Lambda \approx 0.7$ apply.

2.3   Dark Energy

The first evidence for the presence of dark energy came, as noted by Freese (2017), from observations of distant supernovae, which appeared to be dimmer than expected. This faintness is attributed to the accelerating expansion of the universe, that is driven by dark energy.

Recently published results from the **Dark Energy Survey** (DES Collaboration et al. 2025) suggest that dark energy may not be constant over time. The DES team compared the expansion history of the universe derived from Type Ia Supernovae (SNe), the standard candles used to measure cosmic distances, with data from Baryonic Acoustic Oscillations (BAO) - imprints of sound waves (pressure waves) from the early universe that serve as a standard ruler to measure the universe's expansion. These findings were also in contrast with previously determined values of Ω_m, obtained from analyzes of the CMB and primordial nucleosynthesis. The results suggest values of $\Omega_m \approx 0.31$ and $H_0 = 67.81 \, \text{km} \, \text{s}^{-1} \text{Mpc}^{-1}$, which are consistent with those gathered by Planck. However, the results obtained from different observational methods (BAO vs. SNe) show non-negligible differences. This discrepancy indicates that more complex models than the standard ΛCDM may be required to fully explain the observed data, as proposed in the article by DES Collaboration et al. (2025).

2.4   The Nature of Dark Matter

According to Freese (2017), there are two main arguments supporting the non-baryonic nature of dark matter. The first comes from the primordial nucleosynthesis. Once deuterium D becomes stable via the reaction $p + n \rightarrow D + \gamma$, other light elements such as helium He and lithium Li can also form. However, the synthesis of heavier elements did not occur until nearly a billion years later, during stellar evolution. In order for the predicted abundances of these light elements to match observations, baryonic matter (ordinary atoms) must constitute only about 5% of the total mass-energy content of the universe. The other comes from the analysis of the CMB.

2.4.1 Cold Dark Matter

Cold dark matter (CDM) refers to particles that move at non-relativistic speeds (much slower than the speed of light) in the early universe. From an early state dominated by fundamental particles, the universe gradually evolved various of structures — galaxies, galaxy clusters, stars, and so on. It is thought that dark matter played a remarkable role in this formation. CMB hints that small irregularities in the distribution of dark matter made the structure creation possible (Dodelson et al. 1996). As stated in the same article, one of the pillars of CDM theory is the theory of inflation, which the universe underwent at approximately $t \approx 10^{-34}$ s. During this extremely brief period, the universe expanded in size by a factor greater than 10^{25}. This rapid expansion is also considered the reason for the universe's observed flatness, corresponding to a total density near the critical value ρ_{crit} (Eq. (2.2)).

2.4.2 Dark Matter Candidates

Previously, some theories suggested that **MACHOs** (Massive Compact Halo Objects) could constitute dark matter. According to this hypothesis, dark matter would be made up of hard-to-detect objects such as faint stars, white dwarfs, neutron stars, brown dwarfs, or primordial black holes. Using HST data, it was estimated that low-mass stars could contribute up to 3% of the Milky Way's total mass, indicating that MACHOs cannot be the primary component of dark matter. Other surveys show that stellar remnants, especially white dwarfs, could account for up to 15% of the Milky Way's dark matter. Other objects mentioned have also been ruled out as the primary component of dark matter, so it must be composed of a different, unknown material (Freese 2017).

The particles that make up dark matter could, for example, be **Weakly Interacting Massive Particles** (**WIMPs**). The relic density of WIMPs, Ω_{WIMP}, is comparable to the dark-matter density, Ω_{DM} (Salucci 2019). WIMPs also arise naturally as a byproduct of certain particle physics theories, as stated by Freese (2017).

Another possible type of a dark-matter particle could be **axions**, which already exist within the framework of particle physics.

It was previously considered that **neutrinos** could be the dark matter particles; however, their relativistic speeds would prevent the formation of gravitational structures, and ordinary neutrinos are also too light to contribute significantly to the total mass budget (Freese 2017).

Dust particles and ordinary (baryonic) matter were also ruled out, as there are not enough heavy elements (produced through stellar nucleosynthesis) to account for the required dark matter content. Furthermore, baryonic matter interacts with electromagnetic radiation, in contrast to dark matter.

2.5   Analytical Scalings of Dark Matter

2.5.1   Virial Theorem

The virial theorem can be used to determine the mass of a stellar system. The virial quantity G of a system composed of N point masses is

$$G = \sum_{i=1}^{N} \tilde{p}_i \cdot \tilde{x}_i^2, \tag{2.5}$$

where $\tilde{p}_i$ and $\tilde{r}_i$ are momentum and position vector of the particles (the original principles were set by Clausius 1870, see also many more modern versions, a practical summary is for example in Mikulášek and Krtička 2005).
Assuming the system is quasi-equilibrial (quasistationary), then $\dot{G} = 0$. For the first time derivative we get

$$\dot{G} = \sum_{i=1}^{N} m_i \left(\dot{\tilde{x}}_i \cdot \dot{\tilde{x}}_i + \tilde{x}_i \cdot \ddot{\tilde{x}}_i \right) = 0, \tag{2.6}$$

where $\dot{\tilde{x}}_i$ is the velocity and $\ddot{\tilde{x}}_i$ is the acceleration of the particles. The first term is

$$\sum_{i=1}^{N} m_i \cdot \dot{\tilde{x}}_i \cdot \dot{\tilde{x}}_i = 2T, \tag{2.7}$$

where T is the average kinetic energy of the system. As for the second term, while denoting $\ddot{\tilde{x}}_i = \tilde{g}_i(\tilde{x}_i)$, it can be expanded as

$$\sum_{i=1}^{N} m_i \cdot \tilde{x}_i \cdot \ddot{\tilde{x}}_i = \sum_{i=1}^{N} m_i \cdot \tilde{x}_i \cdot \tilde{g}_i(\tilde{x}_i) = \sum_{i=1}^{N} m_i \cdot \tilde{x}_i \cdot \sum_{j=1, j \neq i}^{N} -G \frac{m_j(\tilde{x}_i - \tilde{x}_j)}{|\tilde{x}_i - \tilde{x}_j|^3}. \tag{2.8}$$

The summation $\sum_{j \neq i}$ takes into account the constraint, that the gravitational interaction cannot act between one and the same particle. The addition of particles and their combination then implies the expansion of Eq. (2.8) as

$$-G \sum_{i=1}^{N} \sum_{j>i} m_i \cdot \tilde{x}_i \cdot \frac{m_j(\tilde{x}_i - \tilde{x}_j)}{|\tilde{x}_i - \tilde{x}_j|^3} + G \sum_{i=1}^{N} \sum_{j<i} m_i \cdot \tilde{x}_i \cdot \frac{m_j(\tilde{x}_i - \tilde{x}_j)}{|\tilde{x}_i - \tilde{x}_j|^3}, \tag{2.9}$$

where the opposite signs originate from the order of particles i, j in the numerator bracket. If the order of the particles in one of the brackets were to be opposite, so would be the sign of corresponding term. By reversing the inequality in the sum of the second term, all of the other i, j indexes also swap. We get

$$-G \left[\sum_{i=1}^{N} \sum_{j>i} m_i \cdot \tilde{x}_i \cdot \frac{m_j(\tilde{x}_i - \tilde{x}_j)}{|\tilde{x}_i - \tilde{x}_j|^3} + \sum_{i=1}^{N} \sum_{j>i} m_j \cdot \tilde{x}_j \cdot \frac{m_i(\tilde{x}_j - \tilde{x}_i)}{|\tilde{x}_j - \tilde{x}_i|^3} \right] =$$

$$-G \left[\sum_{i=1}^{N} \sum_{j>i} m_i \cdot \tilde{x}_i \cdot \frac{m_j(\tilde{x}_i - \tilde{x}_j)}{|\tilde{x}_i - \tilde{x}_j|^3} - \sum_{i=1}^{N} \sum_{j>i} m_j \cdot \tilde{x}_j \cdot \frac{m_i(\tilde{x}_i - \tilde{x}_j)}{|\tilde{x}_i - \tilde{x}_j|^3} \right] =$$

$$-G\sum_{i=1}^{N}\sum_{j>i} m_i \cdot m_j \cdot \frac{(\tilde{x}_i - \tilde{x}_j)}{|\tilde{x}_i - \tilde{x}_j|^3} \cdot (\tilde{x}_i - \tilde{x}_j) = -G\sum_{i=1}^{N}\sum_{j>i} \frac{m_i \cdot m_j}{|\tilde{x}_i - \tilde{x}_j|}. \qquad (2.10)$$

It can be seen that the Eq. (2.10) expresses the total potential energy of the system. Equation (2.6) can be rewritten as the virial theorem

$$2T + V = 0, \qquad (2.11)$$

where V is the potential energy.

2.5.2 Virial Mass and Radius

The virial mass, m_{vir}, is the mass of a system to which the virial theorem applies, contained within the virial radius, r_{vir}. The virial radius is defined, for example, by Kravtsov (2013) as the radius r_{200} within which the average density is 200 times the critical density of the universe, ρ_{crit}. The corresponding virial mass is defined as $m_{200} = (4/3)\,\pi\,200\,\rho_{\mathrm{crit}}\,r_{200}^3$.

2.5.3 Jeans equations

The Jeans equations can be understood as an analogy to the Euler hydrodynamic equations for a stellar system. For an introduction to the formalism of their derivation, see, e.g., Kurfürst (2024). The first one, the **continuity equation**, is given by

$$\frac{\partial n}{\partial t} + \sum_{i=1}^{3} \frac{\partial\,(n\langle v_i\rangle)}{\partial x_i} = 0, \qquad (2.12)$$

where $n(t,\mathbf{x})$ is the number density of bodies involved and $\langle v_i\rangle$ is the mean value of the i-th velocity component. The Jeans **momentum equation** (collisionless analogue to the Newton's second law) has the form

$$\frac{\partial\,(n\langle v_i\rangle)}{\partial t} + \sum_{j=1}^{3} \frac{\partial\,(n\langle v_i v_j\rangle)}{\partial x_j} = -n\frac{\partial\Phi}{\partial x_i}, \qquad (2.13)$$

where Φ is the gravitational potential. The second term on the left-hand side represents the divergence of the velocity tensor, where we can introduce the velocity dispersion

$$\sigma_{ij}^2 = \langle v_i v_j\rangle - \langle v_i\rangle\langle v_j\rangle. \qquad (2.14)$$

By substituting Eq. (2.14) into Eq. (2.13), expanding the derivatives and subtracting Eq. (2.12), we can rewrite the Jeans momentum equation in terms of mean motion and dispersion, as

$$n\frac{\partial\langle v_i\rangle}{\partial t} + n\sum_{j=1}^{3} \langle v_j\rangle\frac{\partial\langle v_i\rangle}{\partial x_j} = -n\frac{\partial\Phi}{\partial x_i} - \sum_{j=1}^{3} \frac{\partial\,(n\sigma_{ij}^2)}{\partial x_j}, \qquad (2.15)$$

where the last term represents an analogy with the pressure gradient term in the Euler momentum equation.

Now, assuming axial symmetry in cylindrical coordinates, where $\frac{\partial}{\partial \phi} = 0$, and spherical symmetry in spherical coordinates, where $\frac{\partial}{\partial \theta} = 0$ and $\frac{\partial}{\partial \phi} = 0$, the divergence of an arbitrary vector **u** in these coordinate systems takes the form

$$\nabla \cdot \mathbf{u}\big|_{\text{cyl}} = \frac{1}{R}\frac{\partial}{\partial R}\left(R\,u_R\right) + \frac{\partial u_z}{\partial z}, \quad \nabla \cdot \mathbf{u}\big|_{\text{spher}} = \frac{1}{r^2}\frac{\partial}{\partial r}\left(r^2 u_r\right). \tag{2.16}$$

Assuming also stationarity, where $\frac{\partial}{\partial t} = 0$, the expanded component form of Eq. (2.13) in **cylindrical coordinates** (for the galactic disk) takes the form:

$$\frac{\partial\left(n\langle v_R^2\rangle\right)}{\partial R} + \frac{\partial\left(n\langle v_R v_z\rangle\right)}{\partial z} + \frac{n\langle v_R^2\rangle}{R} - \frac{n\langle v_\phi^2\rangle}{R} = -n\frac{\partial\Phi}{\partial R}, \tag{2.17}$$

$$\frac{\partial\left(n\langle v_R v_\phi\rangle\right)}{\partial R} + \frac{\partial\left(n\langle v_\phi v_z\rangle\right)}{\partial z} + \frac{2n\langle v_R v_\phi\rangle}{R} = 0, \tag{2.18}$$

$$\frac{\partial\left(n\langle v_R v_z\rangle\right)}{\partial R} + \frac{\partial\left(n\langle v_z^2\rangle\right)}{\partial z} + \frac{n\langle v_R v_z\rangle}{R} = -n\frac{\partial\Phi}{\partial z}, \tag{2.19}$$

where the last terms on the left-hand sides of Eqs. (2.17) and (2.18) represent the centrifugal and Coriolis forces, respectively.

Again assuming stationarity, the expanded form in **spherical coordinates** (for an elliptical galaxy or a dark-matter halo) is

$$\frac{\partial\left(n\langle v_r^2\rangle\right)}{\partial r} + \frac{2n\langle v_r^2\rangle}{r} - \frac{n\langle v_\theta^2\rangle}{r} - \frac{n\langle v_\phi^2\rangle}{r} = -n\frac{\partial\Phi}{\partial r}, \tag{2.20}$$

where the last two terms on the left-hand side represent the centrifugal force contributions in the angular directions.

We can also introduce a parameter β, which quantifies the orbital anisotropy (i.e., the difference in the velocity distribution between radial and tangential directions) and, in the spherical case, it is given by

$$\beta \equiv \frac{2\sigma_r^2 - \sigma_\theta^2 - \sigma_\phi^2}{2\sigma_r^2} = \frac{2\langle v_r^2\rangle - \langle v_\theta^2\rangle - \langle v_\phi^2\rangle}{2\langle v_r^2\rangle}, \tag{2.21}$$

where the first expression on the right-hand side is the general definition (as used, for example, by Kowalczyk et al. (2017)), while the second term applies in the case of a non-rotating system. Using β, we can rewrite Eq. (2.20) as

$$\frac{\partial\left(n\langle v_r^2\rangle\right)}{\partial r} + \frac{2\beta\,n\langle v_r^2\rangle}{r} = -n\frac{\partial\Phi}{\partial r}. \tag{2.22}$$

The mass profile M_r (i.e., the mass enclosed within radius r) can be expressed in terms of the number density of stars n, the radial velocity dispersion σ_r, and the anisotropy parameter β. In spherical symmetry, the gravitational potential satisfies

$$\frac{d\Phi(r)}{dr} = \frac{GM_r}{r^2}, \tag{2.23}$$

and the mass profile can then be written as

$$M_r = -\frac{r\sigma_r^2}{G}\left[\frac{\mathrm{d}\ln(n\sigma_r^2)}{\mathrm{d}\ln r} + 2\beta\right],\tag{2.24}$$

as given by Binney and Tremaine (1987).

The simplest assumption for a dark-matter halo is that it is spherical with only radially dependent quantities, so its total gravitational potential is also spherical (since the mass is dominated by the halo outside the disk). Under this assumption, we can adopt the mass profile M_r as shows Eq. (2.24).

2.6 Detection of Dark Matter

2.6.1 Measuring Rotational Velocities

One way to observe dark matter, as I previously mentioned in Sect. 1.4.1, is by measuring the rotational velocities of galaxies. The majority of galaxies exhibit similarity in their rotation curves, as shown in Fig. 2.3. Specifically, the outer parts of these curves do not behave as expected based on the concentration of luminous matter.
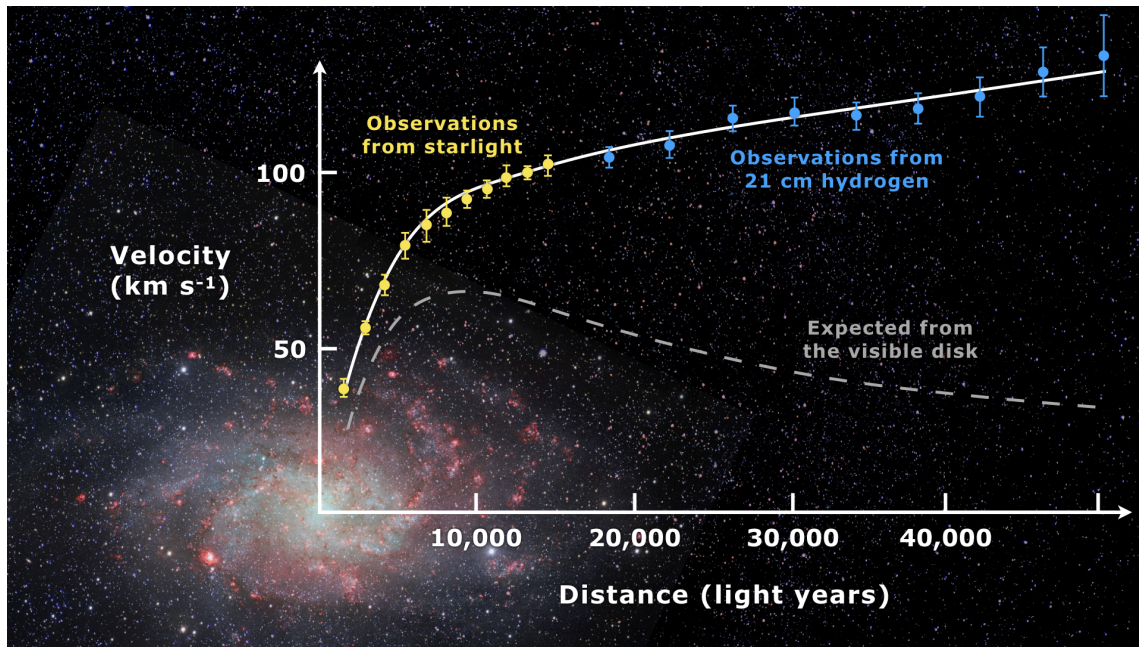
Figure 2.3: *Rotation curve of spiral galaxy Messier 33 (Leo 2018).*

2.6.2 Gravitational Lensing

Another method used for detecting large clumps of dark matter is through observations of gravitational lensing. When a massive object lies between an observer and a distant light source, such as a galaxy, the light from the source is bent by the gravitational field of the massive object. This effect results in a distorted image for the observer, and by analyzing the shapes and other characteristics of the warped image, one can calculate the mass of the object that caused the light to bend. This phenomenon is illustrated in Fig. 2.4.

According to Pfrommer (2022), we can distinguish between two main gravitational lensing types. **Strong lensing** is characterized by a significant and visible distortion of the distant object. This type of lensing can result in multiple images of the object or a so-called Einstein ring (Fig. 2.5). **Weak lensing** on the other hand, causes milder deformations and can be detected only by analyzing a larger number of objects (galaxies).

Figure 2.4: *Gravitational lensing around galaxy cluster CL0024+17. The yellow galaxies are part of the cluster, while the blue, distorted ones are more distant (NASA/ESA/M.J. Jee 2007).*

Figure 2.5: *Einstein ring in the galaxy cluster SMACS J0028.2−7537 (ESA/Webb et al. 2025). The image shows two galaxies: a closer galaxy at the center and a much more distant background galaxy, whose light is gravitationally lensed into a ring-like structure around the central galaxy.*
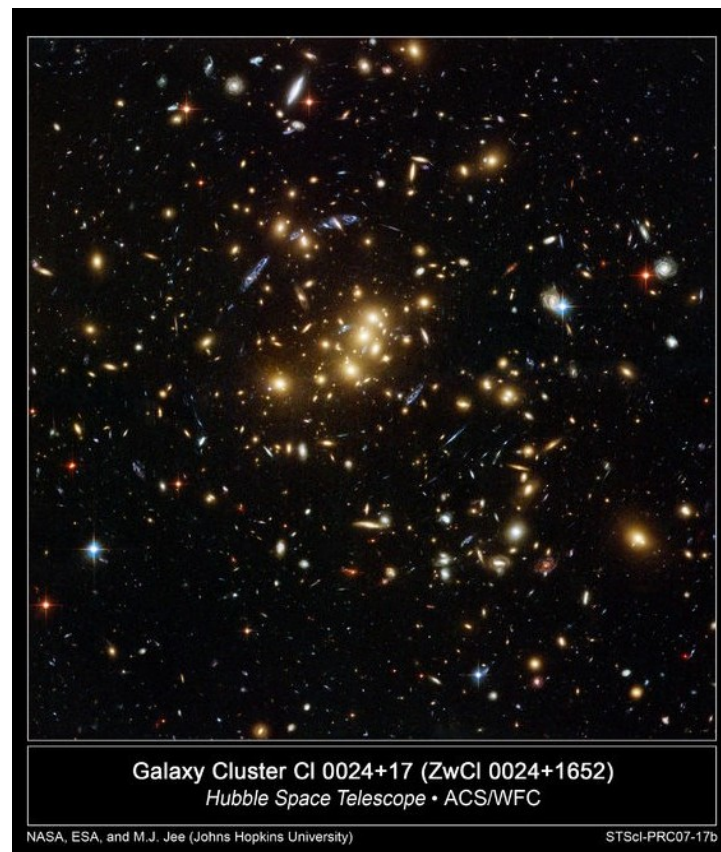
2.6.3   Dark-Matter Detectors

The **XENONnT** detector, located in Italy, is designed to detect WIMPs, which are leading candidates for dark matter (XENON Collaboration and Others 2024). When the hypothetical dark-matter particle (WIMP) passes through the detector, it may interact with a xenon nucleus in the liquid xenon tank. This interaction can cause the nucleus to recoil, producing both scintillation light (a flash of ultraviolet light) and ionization electrons, which are detected to infer the presence of a WIMP. The predecessors of this detector were **XENON10**, **XENON100**, and **XENON1T**, each achieving progressively greater sensitivity and setting increasingly lower limits on the WIMP−nucleon cross section for hypothetical dark-matter particles, as shown in Fig. 2.6.

Another dark-matter detector is **ADMX** (Axion Dark Matter eXperiment), which is designed to detect axion and is operated at the University of Washington, USA (Khatiwada et al. 2021). In the presence of a strong magnetic field, axions can convert into microwave photons. These photons are then detected using an ultra-sensitive microwave cavity and amplifiers cooled to cryogenic temperatures.

CASPEr (Cosmic Axion Spin Precession Experiment) is another detector that focuses on axions, developed at Johannes Gutenberg University Mainz in Germany (Garcon et al. 2017). CASPEr aims to detect tiny changes in the spin of atomic nuclei, which could be induced by the interaction of axions with nuclear spins.
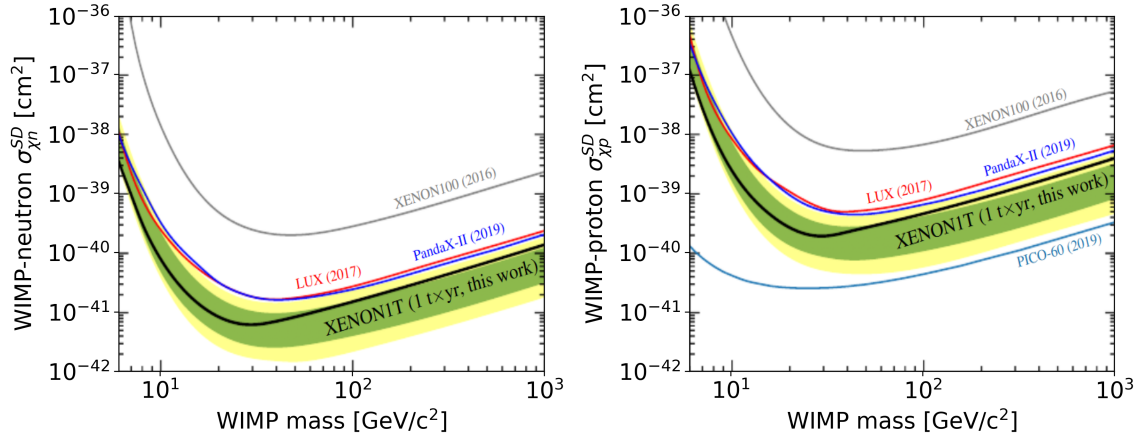
Figure 2.6: *The graphs show the upper limit for a WIMP-neutron (left) and WIMP-proton (right) cross section σ. The green (1σ) and yellow (2σ) bands, show the expected sensitivity of the XENON1T experiment (Aprile and Others 2019).*

2.7 Alternative Theory - MOND (Modified Newtonian Dynamics)

Some members of the scientific community prefer another solution than dark matter to the dark gravity problem. Modified Newtonian dynamics theory, introduced by Milgrom (1983b) proposes an adjustment to the Newton's second law as

$$F_N = m \mu \left(\frac{a}{a_0} \right) a, \tag{2.25}$$

where F_N is the Newtonian gravitational force, m is the mass of the gravitating object, $\mu(x)$ is the so-called "interpolating function" and $a_0 \approx 1.2 \cdot 10^{-8} \, \text{cm s}^{-2}$ according to Milgrom (1983a). The values of $\mu(x)$ are limited to

$$\mu(x) \rightarrow 1 \qquad \text{for} \qquad x \gg 1, \tag{2.26}$$

$$\mu(x) \rightarrow x \qquad \text{for} \qquad x \ll 1. \tag{2.27}$$

This is satisfied by, for example,

$$\mu(x) = \frac{1}{1 + x^{-1}}, \tag{2.28}$$

$$\mu(x) = \frac{1}{\sqrt{1 + x^{-2}}}, \tag{2.29}$$

$$\mu(x) = 1 - e^{-x}. \tag{2.30}$$

Although MOND explains galaxy the rotation curves quite well, it fails to account for gravitational lensing. In some cases, MOND is consistent with observations of weak gravitational lensing; however, the theory does not hold for strong lensing (Mortlock and Turner 2001).

3. Data Collection and Analysis

3.1 Chosen Galaxies

The articles by Rubin et al. (1980) and van Albada et al. (1985) inspired my selection of galaxies for this thesis - several of the galaxies we have chosen are also examined in their studies. I wanted to include diverse types of spiral galaxies. The list of selected spiral galaxies is shown in Tab. 3.1. The types and luminosity classes listed in the table are of the NASA/IPAC Extragalactic Database and the $Y_\odot$ is from the SPARC database, as specified later. We have also included one irregular dwarf galaxy (NGC 2366).

Table 3.1: *Chosen galaxies and their specifications.*

Name	Type	Luminosity class	Distance (Mpc)
NGC 2998	SAB(rs)c	I	59 ± 2
NGC 1705	SA0	-	5.3 ± 0.2
NGC 5371	SAB(rs)bc	II-III	27 ± 1
NGC 3198	SB(rs)c	I-II	12.8 ± 0.4
NGC 2366	IB(s)m	IV-V	3.2 ± 0.2
NGC 2903	SAB(rs)bc	I-II	8.0 ± 0.4
NGC 4321	SAB(s)bc	I	16.1 ± 0.4

3.1.1 Galaxy observation

For the galaxies NGC 2998 and NGC 4321, the plan was to use images taken with the Masaryk University AZ800 telescope in Ždánice to obtain surface brightness profiles. For each galaxy, approximately 10 frames were captured. For processing and correcting the frames we used **SIPS** (Scientific Image Processing System), which is available on the Moravian Instruments website. You can see the resulting images in Figs. 3.1 and 3.2. The Masaryk University telescope in Ždánice is equipped with a CMOS (Complementary Metal–Oxide–Semiconductor) camera. This device is similar to its predecessor CCD (charge-coupled device). CMOS sensors are used in astronomy, particularly in photometry and astrophotography. The principle of operation of the sensor is converting incoming light (an image) into electronic signals by photodiodes. The number of these photodiodes implies the resolution (pixel) of the sensor, where with higher resolution, the output image detail quality is also higher.

Figure 3.1: *A stacked image of Messier 100 taken with the Masaryk University telescope AZ800 in Ždánice. The individual frames were captured by Prokop Ohlídal.*

Figure 3.2: *A stacked image of NGC 2998 taken with the Masaryk University telescope AZ800 in Ždánice. The individual frames were captured by Prokop Ohlídal.*

We then obtained the surface brightness profiles by fitting isophotes using the Photutils library for Python, developed by Bradley et al. (2024). However, due to the poor quality and noise in the data, which may been caused by non-ideal conditions during the observations, we ultimately did not use these profiles in this thesis and instead relied on the surface brightness profiles measured by the Spitzer Space Telescope.

3.1.2 The SPARC Database

The **SPARC** (Spitzer Photometry & Accurate Rotation Curves) database contains data for 175 spiral and irregular galaxies and was introduced by Lelli et al. (2016). The rotation curves are derived from previous works (using HI and Hα data), and the photometry was obtained from the **Spitzer Space Telescope**. All of the galaxies we have chosen in this section, except for NGC 4321, are listed in this database.

For the galaxies in this database, Li et al. (2020) presented a catalog of dark-matter halo models. Depending on which model best fits each galaxy (and has the lowest value of χ^2), we used the corresponding $Y_\odot$ from their parameters in this thesis, as shown in Tab. 3.2.

Table 3.2: *Sparc galaxies' $Y_\odot$ and corresponding halo model.*

Name	Mass-to-light ratio $Y_\odot$	Halo models
NGC 2998	0.39	DC14-Flat
NGC 1705	0.49	pISO-Flat
NGC 5371	0.42	pISO-Flat
NGC 3198	0.45	Lucky13-Flat
NGC 2366	0.35	DC14-Flat
NGC 2903	0.44	DC14-Flat

From this database, we obtained the surface brightness (μ_{disk}) profiles and the mentioned rotation curves for the galaxies. The values are listed in Tabs. 8, 9, 10, 11, 12, 13, in the Appendix.

3.2 Surface Brightness Profiles and Corresponding Rotation Curve Models

Apart from others, the Python packages used in this thesis include NumPy, SciPy, Astropy, Matplotlib and galpy.

The surface brightness μ_{disk} (I) of a galaxy can be recalculated into different units. The conversion from linear to logaritmic units can be performed using the relation from Li et al. (2017)

$$\mu\,[\text{mag/arcsec}^2] = M_\odot + 21.572 - 2.5\log_{10} I\,[L_\odot/\text{pc}^2], \tag{3.1}$$

where $M_\odot$ and $L_\odot$ are the absolute magnitude and luminosity of the Sun in the relevant band. For $3.6\,\mu$m the $M_\odot = 3.24\,$mag (Oh et al. 2008). The surface brightness profiles for the chosen galaxies are shown in Fig. 3.3.

The luminosity profile can be interpolated by a spline function (using *SciPy*). That way the luminosity can be estimated for any radius. Assuming a constant mass-to-light ratio $Y_\odot$, the rotation curve can be modeled, based on the lumious parts of the galaxy. To model the gravitational potential (axisymmetric thin disk), *galpy* can be used. To use this function, the parameter $\Sigma(r)$ is needed, which is the surface mass density and can be calculated by multiplying $Y_\odot$ and $\mu_{\text{disk}}(r)$. And lastly, using *galpy*'s *diskpot.vcirc* the circular velocity can be calculated as

$$v_c(R) = \sqrt{R \cdot \frac{\partial \Phi}{\partial R}}. \tag{3.2}$$

These steps were done using a Python code (Listing 1). The results are shown in Fig. 3.4.
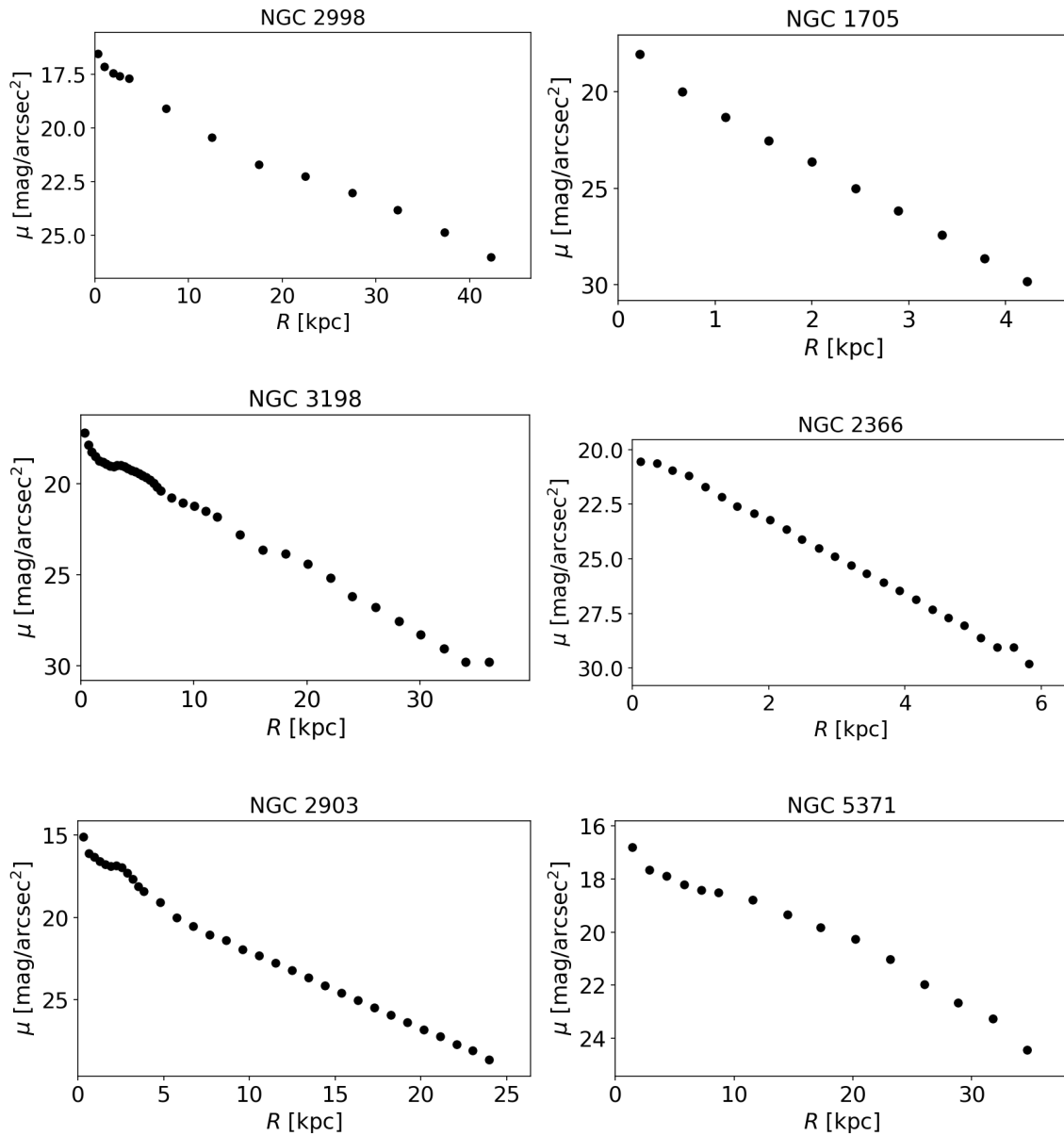
Figure 3.3: *Surface brightness profiles of the galaxies (from SPARC).*
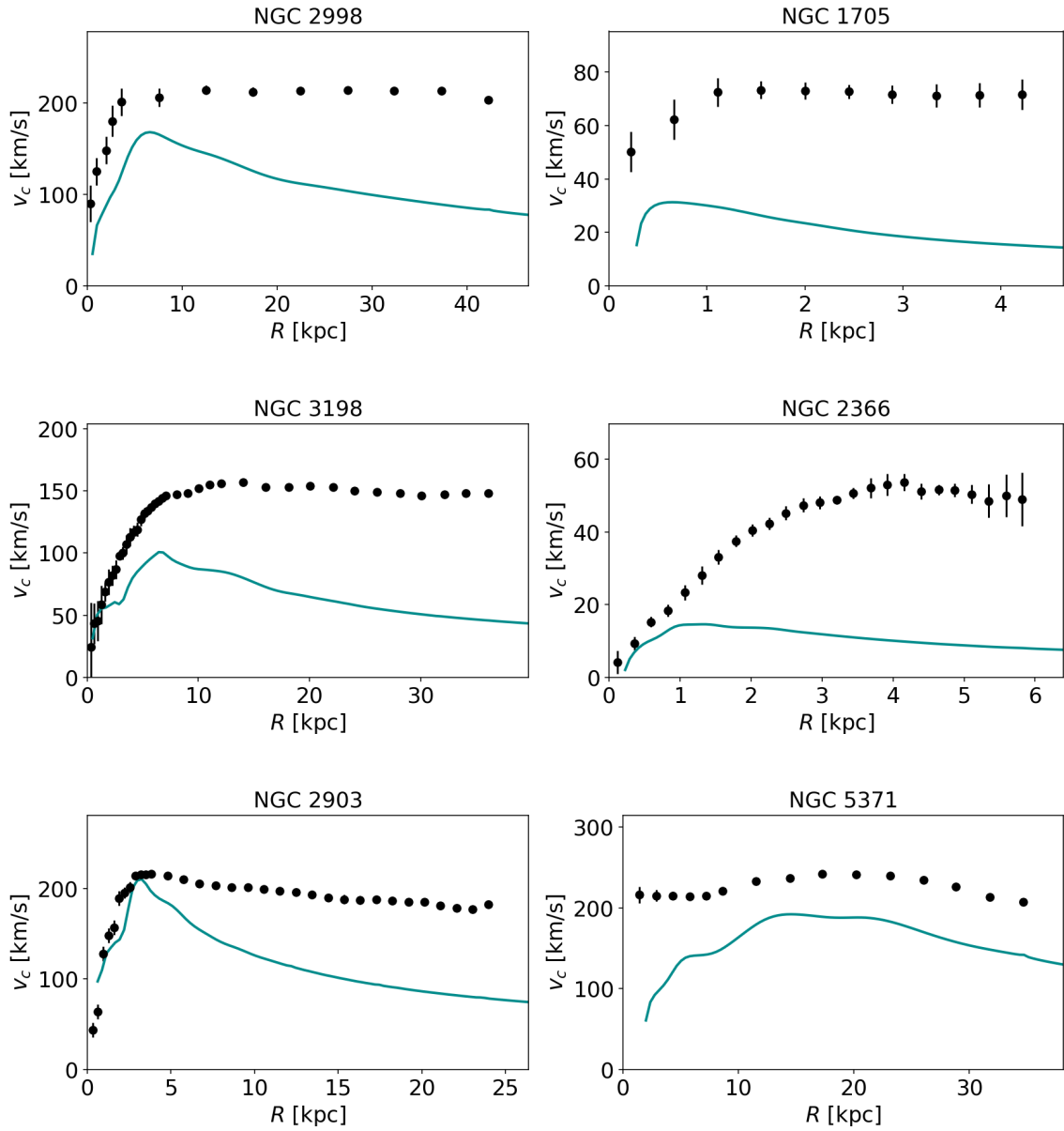
Figure 3.4: *Rotation curves of the galaxies (black points) and modeled rotation curves from the luminosity profile (teal curve) from the SPARC data.*

3.2.1 Galpy

Galpy is a Python library, developed by Jo Bovy from the University of Toronto (Bovy 2015) which is used for galactic dynamics. Aside from many other functions, from its *galpy.potential*, one can import various potentials, such as the Miyamoto-Nagai, Kuzmin, or axisymmetric razor-thin disk potential.

3.3   Obtaining Dark-Matter Density

For the observed circular velocity v_c, the following relation holds

$$v_c^2 = v_{\text{disk}}^2 + v_{\text{DM}}^2 + \dots, \tag{3.3}$$

where v_{disk} and v_{DM} are the contributions from the stellar disk and dark-matter halo, respectively. Using the data shown in Fig. 3.4, the dark-matter contribution can be estimated (neglecting gas and bulge components) as

$$v_{\text{DM}} = \sqrt{v_c^2 - v_{\text{disk}}^2}, \tag{3.4}$$

as used, for example, in Dehnen et al. (2006).

3.3.1   Using Poisson's equation

The Poisson's equation (1.20) takes in spherical symmetry form

$$\frac{1}{r^2}\frac{\mathrm{d}}{\mathrm{d}r}\left(r^2\frac{\mathrm{d}\Phi}{\mathrm{d}r}\right) = 4\pi G\rho(r). \tag{3.5}$$

And because Eq. (1.32) holds, the dark-matter density ρ_{DM} can be approximately obtained as

$$\rho_{\text{DM}}(r) = \frac{1}{4\pi G}\left[\frac{1}{r^2}\frac{\mathrm{d}}{\mathrm{d}r}\left(rv_{\text{DM}}^2(r)\right)\right]. \tag{3.6}$$

By applying this equation, we obtained ρ_{DM} for the galaxies. The resulting curves exhibit a clear trend, despite being somewhat jagged. The reason for the irregularities in the calculated density is the large statistical noise caused by applying the exact mathematical method (Poisson's equation) to the set of measured data, along with the relatively low number of data points. The trend can be modeled using a broken power-law profile, given by

$$\rho_{\text{DM, fit}} = A\left(\frac{r}{r_b}\right)^{\alpha_1}\left[0.5\left(1+\left(\frac{r}{r_b}\right)^{1/\Delta}\right)\right]^{(\alpha_1-\alpha_2)\Delta}, \tag{3.7}$$

where A is a constant (amplitude), r is the radial distance, r_b is the radial distance of the power-law break, α_1 and α_2 are the slope indexes inside and outside the breakpoint, and the Δ parameter sets the "smoothness" of the slope change, as similarly used by Kurfürst et al. (2024). The obtained ρ_{DM} curves and corresponding models are shown in Fig. 3.5 and the parameters of the fits are written in Tab. 3.3.
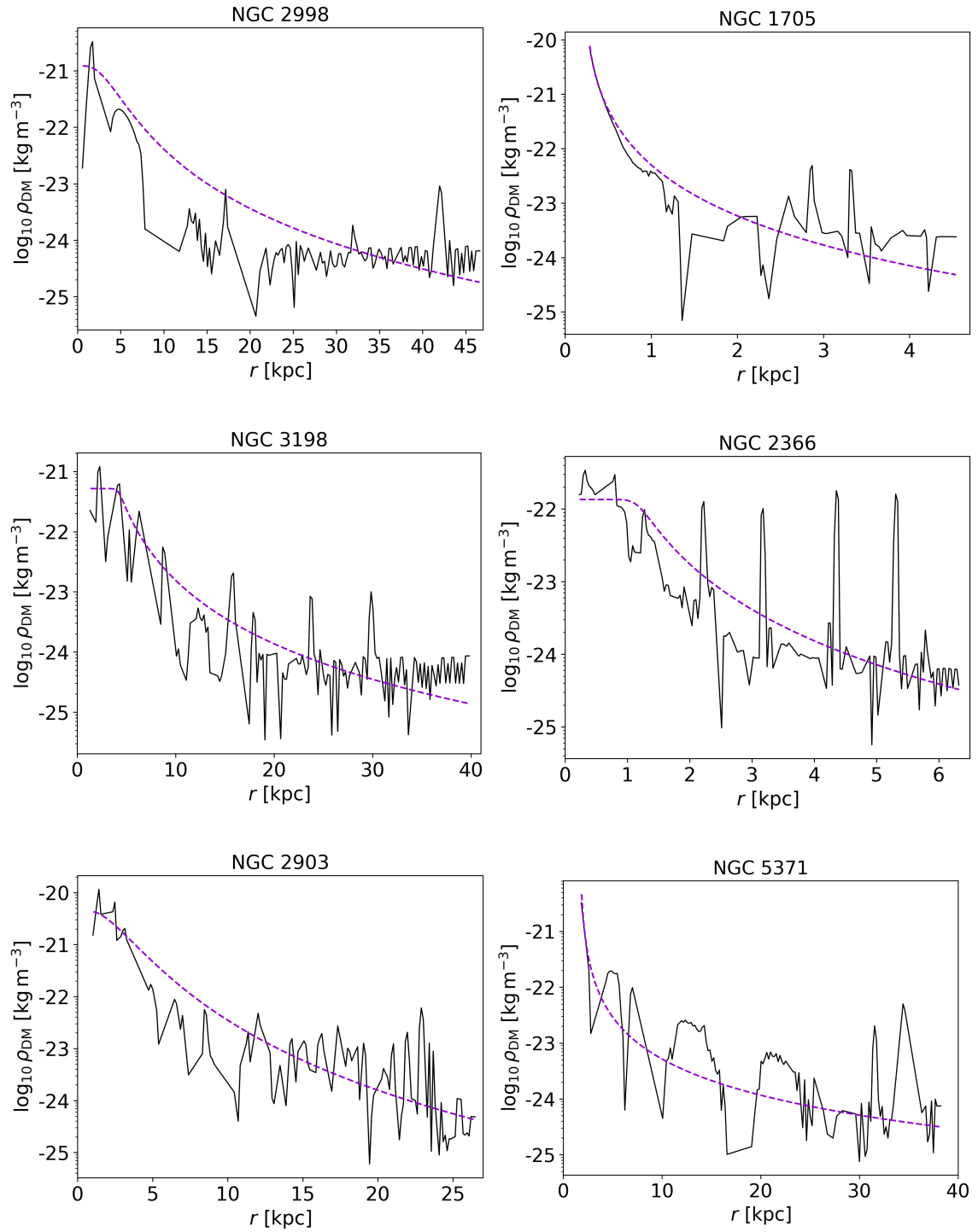
Figure 3.5: *Dark-matter density calculated using Eq. (3.5) (black solid line) and a density modeled using Eq. (3.7) (purple dashed line).*

Table 3.3: *Parameters obtained by fitting $\rho_{DM,\,fit}$ from Eq. 3.7 to the ρ_{DM} curves.*

Galaxy name	A $(\mathrm{kg\,m^{-3}})$	r_b (m)	α_1	α_2	Δ
NGC 2998	$4.40 \cdot 10^{-22}$	$9.61 \cdot 10^{19}$	-0.04	-3.51	0.42
NGC 1705	$6.15 \cdot 10^{-22}$	$1.48 \cdot 10^{19}$	-0.91	-3.09	1.25
NGC 5371	$1.32 \cdot 10^{-21}$	$7.05 \cdot 10^{18}$	0.00	-1.94	0.97
NGC 3198	$4.48 \cdot 10^{-22}$	$8.84 \cdot 10^{19}$	-0.06	-3.17	0.07
NGC 2366	$1.11 \cdot 10^{-22}$	$2.90 \cdot 10^{19}$	-0.06	-3.22	0.09
NGC 2903	$5.39 \cdot 10^{-22}$	$1.15 \cdot 10^{20}$	-0.83	-4.32	0.63

We can calculate the total mass of the dark-matter halo by summing the masses of individual spherical shells. The mass of such a shell can be determined as

$$M_{\mathrm{shell}} = \frac{4}{3}\pi\rho_r(r_2^3 - r_1^3). \tag{3.8}$$

Tab. 3.4 shows the halo-mass values we obtained this way.

Table 3.4: *Calculated values of dark-matter halo masses.*

Galaxy name	Halo mass (kg)
NGC 2998	$1.899 \cdot 10^{40}$
NGC 1705	$7.564 \cdot 10^{37}$
NGC 5371	$4.261 \cdot 10^{40}$
NGC 3198	$1.521 \cdot 10^{40}$
NGC 2366	$2.891 \cdot 10^{38}$
NGC 2903	$3.035 \cdot 10^{40}$

3.3.2   Using Halo Models

Another way to obtain the dark-matter density, is to use an already existing halo model. By fitting $v_{DM}(r)$ with modelled curves derived from the potentials, necessary parameters can be obtained.
We used three models, specifically the NFW model, the Hernquist model and the isothermal sphere (pISO) model, already introduced in Sect. 1.4.4. In *galpy* they are defined as

$$\rho(r)_{\mathrm{NFW}} = \frac{\mathrm{amp}}{4\pi a^3}\frac{1}{(r/a)(1+r/a)^2}, \tag{3.9}$$

$$\rho(r)_{\mathrm{Hernquist}} = \frac{\mathrm{amp}}{4\pi a^3}\frac{1}{(r/a)(1+r/a)^3}, \tag{3.10}$$

$$\rho(r)_{\mathrm{pISO}} = \frac{\mathrm{amp}}{4\pi a^3}\frac{1}{1+(r/a)^2}, \tag{3.11}$$

where amp is the amplitude and *a* is the scale radius (core radius for pISO). The fitting was done by a python script (Listing 2) and is shown in Fig. 3.6 and the obtained parameter values are written in Tabs. 3.5, 3.6 and 3.7. *Galpy* uses internal units, so the

parameter values need to be properly rescaled, which explains the unusual units of the parameters in the tables. After obtaining the parameters, we plotted the density ρ_{DM} for each of the models, again by using *galpy*'s function *evaluateDensities*. The resulting density plots are shown in Figs. 3.7, 3.8 and 3.9.

We did not attempt to model the v_{DM} curve for the galaxy NGC 5371, as it does not resemble any of the halo models we used, as you can see in Fig. 3.6.

Table 3.5: *NFW halo model parameters from fitting to v_{DM} curves.*

Galaxy name	amp $[0.3 \cdot 10^{10} \ M_{\odot}]$	a [8 kpc]
NGC 2998	7.737	18.588
NGC 1705	0.084	1.440
NGC 3198	3.987	16.733
NGC 2366	0.739	13.691
NGC 2903	6.279	17.701

Table 3.6: *pISO halo model parameters from fitting to v_{DM} curves.*

Galaxy name	amp $[0.3 \cdot 10^{10} \ M_{\odot}]$	a [8 kpc]
NGC 2998	0.192	2.029
NGC 1705	0.003	0.223
NGC 3198	0.165	2.781
NGC 2366	0.015	1.440
NGC 2903	0.238	2.719

Table 3.7: *Hernquist halo model parameters from fitting to v_{DM} curves.*

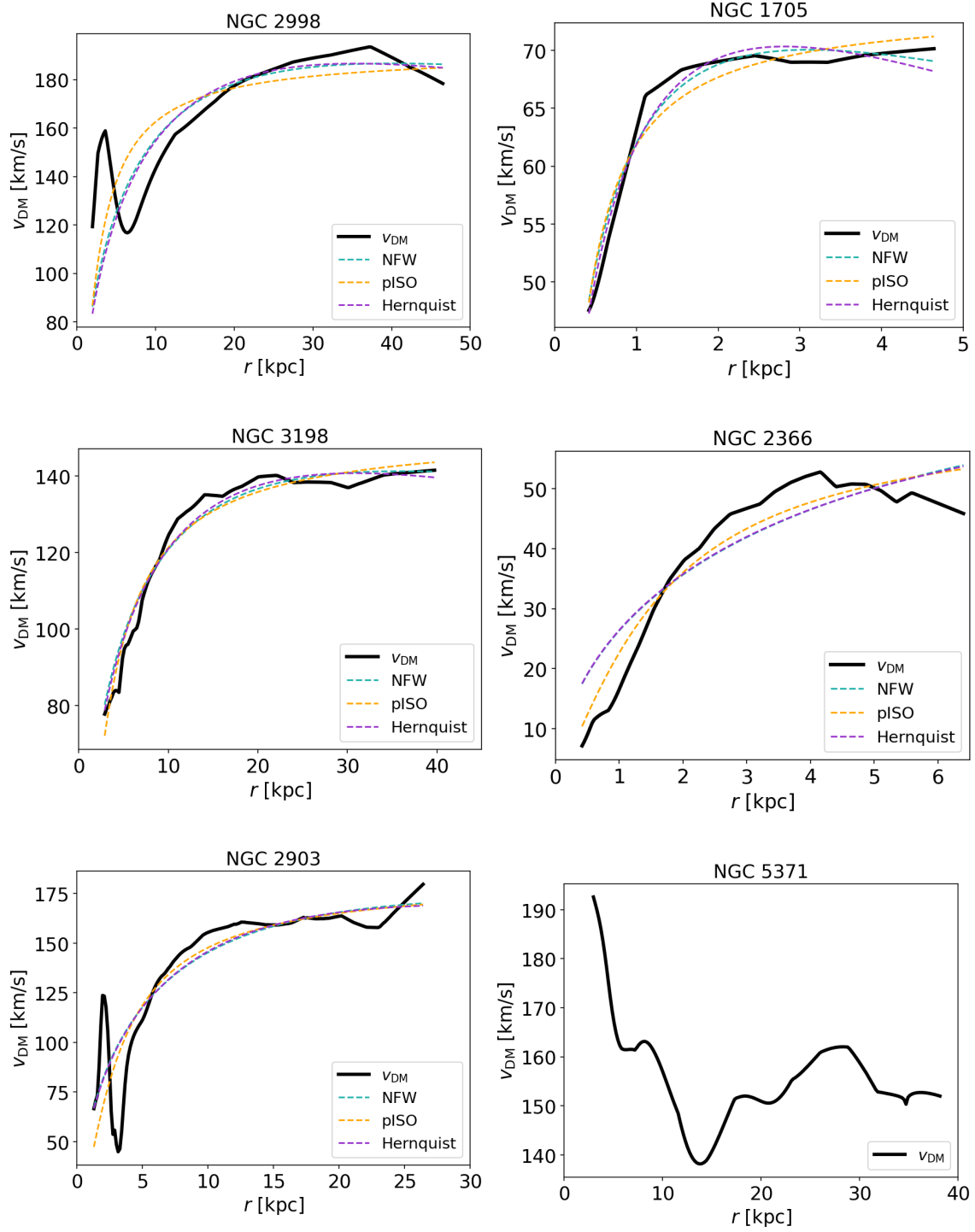| Galaxy name	amp $[0.3 \cdot 10^{10} \ M_{\odot}]$	a [8 kpc]
NGC 2998	25.458	35.381
NGC 1705	0.288	2.815
NGC 3198	12.635	30.888
NGC 2366	1.743	20.969
NGC 2903	18.109	30.581

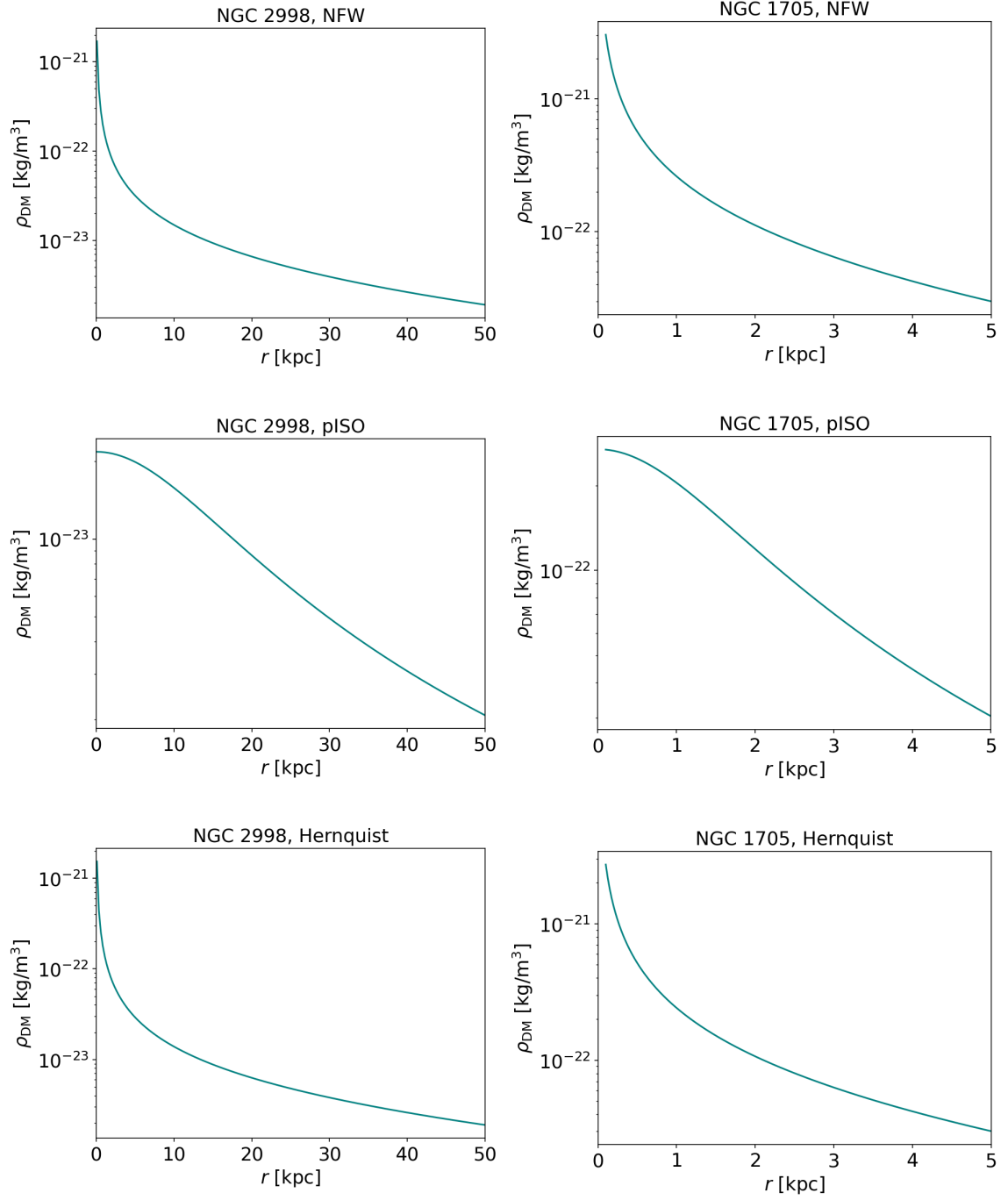Figure 3.6: *Curves of $v_{DM}(r)$ fitted by the three different halo models.*

Figure 3.7: *Dark-matter densities $\rho_{DM}(r)$ obtained from the models for NGC 2998 and NGC 1705.*
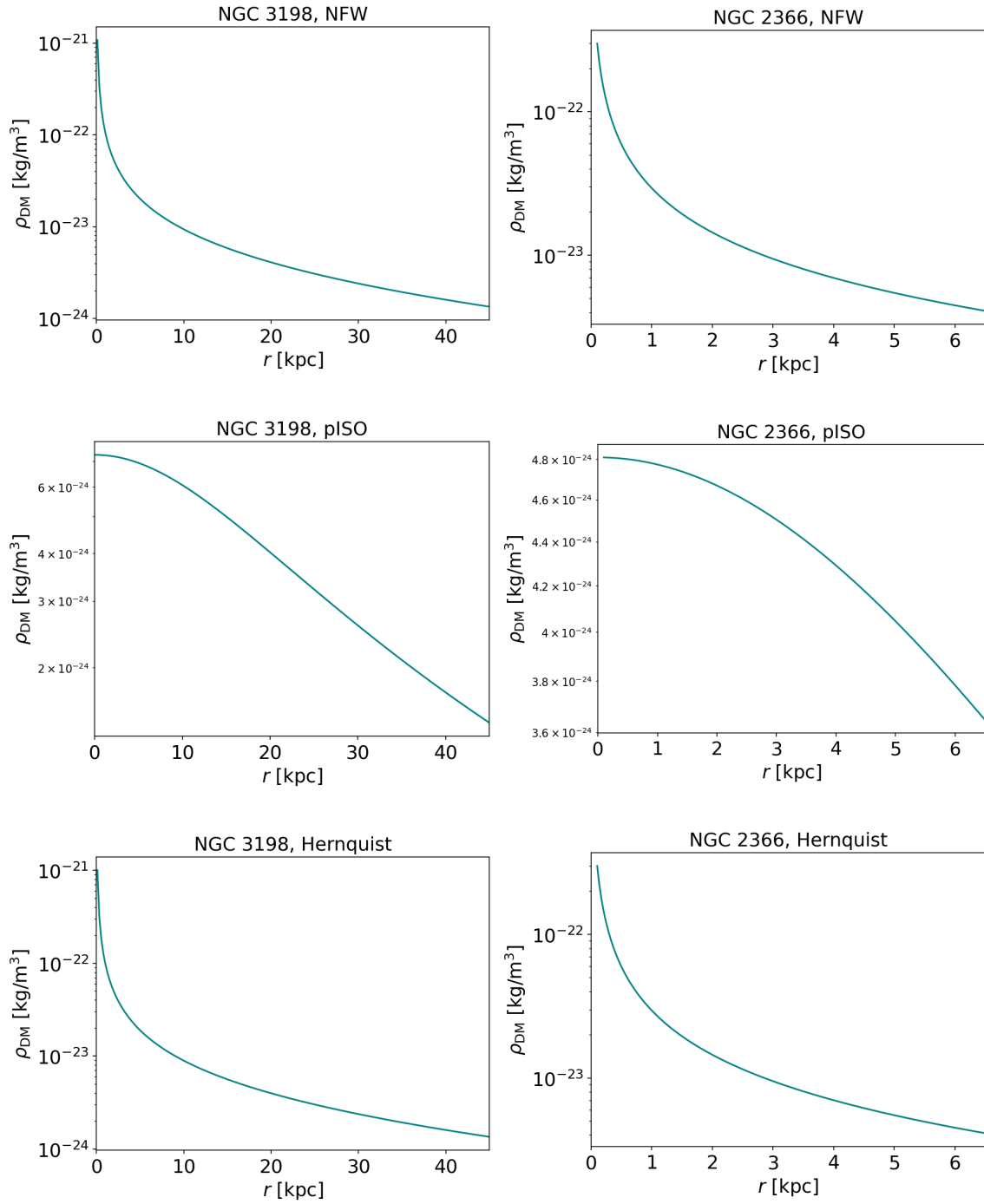
Figure 3.8: *Dark-matter densities ρ_{DM}(r) obtained from the models for NGC 3198 and NGC 2366.*
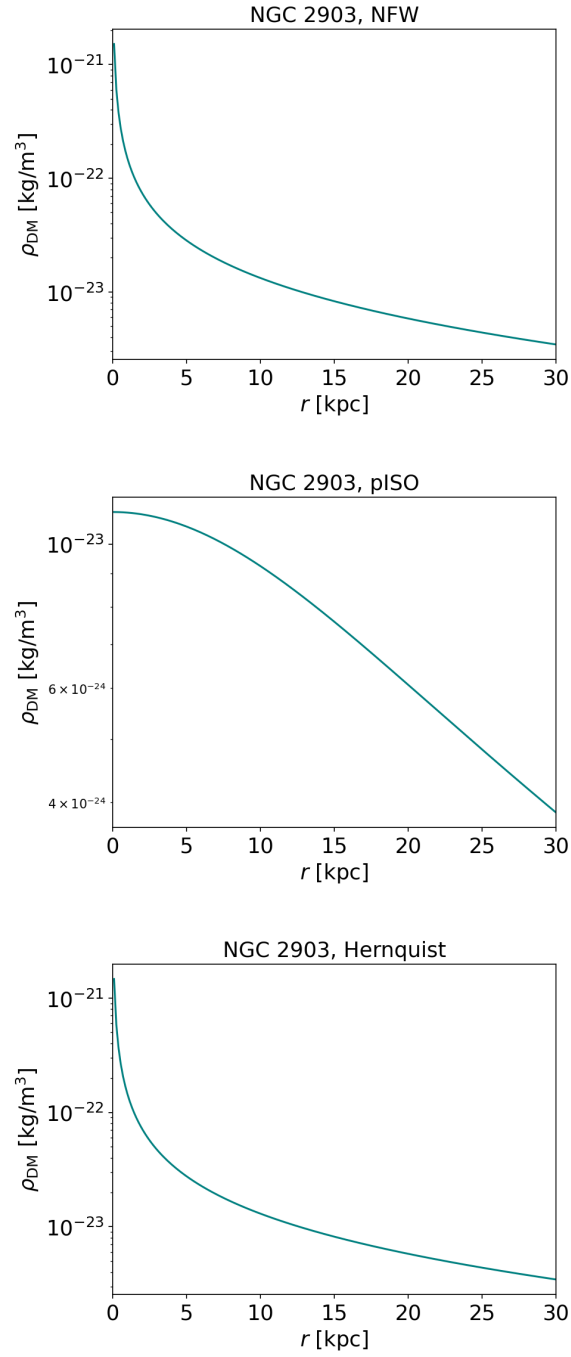
Figure 3.9: *Dark-matter densities $\rho_{DM}(r)$ obtained from the models for NGC 2903.*

3.4   Discussion

After obtaining the necessary data from the SPARC database, we modeled the rotation curves based on the surface brightness of the galaxies and compared them with the observed rotation curves. Fig. 3.4 clearly shows that the disk mass alone cannot account for the gravitational pull indicated by the rotation curves, implying the presence of dark matter. Using Eq. (3.4), we derived the 'dark matter' component of the rotation curves. We then applied two different approaches to determine the dark matter density in the galaxies. It should be noted, that for simplicity, we used the assumption of spherical symmetry for all of the galaxies, which might not hold well, especially for the irregular galaxy NGC 2366.

The first approach uses Eq. (3.6), derived from Poisson's equation under the assumption of spherical symmetry. The resulting dark matter density curves were modeled using the broken power-law profile described in Eq. (3.7). The curves and corresponding fits are shown in Fig. 3.5. While it is visible that small irregularities or noise in the v_{DM} curve can lead to larger changes in the calculated density, the overall trend remains clearly identifiable. The dark-matter density profile of the irregular galaxy NGC 2366, which we obtained through this method (Fig. 3.5), shows four prominent peaks. This could be an indicator of denser regions, where the halo could form compact shells or lodes. It is also possible that the peaks are caused by noise and are just a coincidence.

The second approach models the v_{DM} curves using established dark matter halo profiles. Specifically, we used the NFW, Hernquist, and pseudo-isothermal models. In the case of NGC 5371, we chose to calculate the dark-matter density only using the method based on Poisson's equation. This decision was made due to the irregular shape of its derived v_{DM} curve, which likely reflects complexities already evident in the luminous component model of the rotation curve (Fig. 3.4). This irregularity would complicate the halo model fit and might lead to misleading parameter values. As for the galaxy NGC 2366, it is noticeable that the halo models — especially the NFW and Hernquist profiles — do not align well with the fitted v_{DM} curve (Fig. 3.6), which could cause inaccurate results.

At first glance, the ρ_{DM} curves calculated using the Poisson's equation exhibit a shape more similar to those derived from the NFW and Hernquist models than to those of the pseudo-isothermal model, which displays a distinctly different profile. On the contrary, the fitted v_{DM} curves in Fig. 3.6 seem to correspond better to the pseudo-isothermal profile. In the article by Bovy and Tremaine (2012), they estimate the dark-matter density in the solar neighbourhood to be approximately $0.3\,\mathrm{GeV/cm}^3$, which is equivalent to $5.35 \cdot 10^{-22}\,\mathrm{kg/m}^3$. Since the Milky Way is also a spiral galaxy, our results appear to be consistent with this value, at least in terms of order of magnitude.

The halo masses obtained from the dark-matter densities are listed in Tab. 3.4. As expected, the galaxy NGC 1705, a compact dwarf galaxy, has the lowest halo mass. The irregular galaxy NGC 2366 also shows a significantly lower value compared to the more massive spiral galaxies.

Conclusions

Through both theoretical discussion and practical analysis, this thesis has illustrated the significance of dark matter in galaxies and galaxy clusters. Although dark matter remains shrouded in mystery, several theories regarding its nature were discussed in the theoretical section. However, this work focused primarily on the consequences of its existence rather than its composition. Regardless of the particles that constitute it, dark matter has played a crucial role in the formation of even the largest structures in the universe and continues to serve as their framework. The existence of dark matter halos is supported by galaxy rotation curves, while additional evidence in galaxy clusters comes from phenomena such as gravitational lensing and mass estimates derived from the virial theorem.

The first chapter is devoted to the theoretical description of galaxies and galaxy clusters, presenting the various galaxy types and the physical laws that govern them. The following chapter focuses on dark matter itself. Among other topics, it describes how dark matter can be detected and what it might be composed of. The final chapter is dedicated to data analysis.

Using observational data from the SPARC database, we demonstrated how certain properties of dark matter halos, such as their density profiles and total mass, can be inferred. We began by modeling the rotation curves based solely on the luminous components of the galaxies, which yielded the expected result: an additional source of mass, beyond the stellar disk, is required. After assuming that the galaxies contain only stellar matter and dark matter, we derived the rotation curves corresponding to the dark-matter contribution alone. Using two different methods, we then determined the dark-matter halo density profiles. Additionally, we used one of these methods to estimate the total mass of the dark-matter halos.

While this study focuses on the stellar and dark matter components, the gas can also influence the dynamics of the galaxies. For future work, more advanced computational methods could be employed. For example, the GADGET code (Springel et al. 2001) could be used to perform N-body simulations.

Appendix

A   Python scripts

```python
import numpy as np
from galpy.util import plot as galpy_plot
import astropy.units as u
from astropy.io import ascii
import matplotlib
matplotlib.use('Agg')
import matplotlib.pyplot as plt
from scipy import interpolate
from galpy.potential import
    AnyAxisymmetricRazorThinDiskPotential

_ERASESTR = " " * 80
_CACHE_BASEDIR = os.path.join(os.getenv('HOME'),
    '.galaxiesbook', 'cache')
_CACHE_VIZIER_DIR = os.path.join(_CACHE_BASEDIR, 'vizier')
_LELLI_VIZIER_NAME = 'J/AJ/152/157'
_MAX_NTRIES = 3

def vizier(cat, filePath, ReadMePath,
    catalogname='catalog.dat', readmename='ReadMe'):
    _download_file_vizier(cat, filePath, catalogname)
    _download_file_vizier(cat, ReadMePath, readmename)
    catfilename = os.path.basename(catalogname)
    with open(ReadMePath, 'r') as readmefile:
        fullreadme = ''.join(readmefile.readlines())
        if catfilename.endswith('.gz') and catfilename not in
            fullreadme:
            try:
                subprocess.check_call(['gunzip', filePath])
            except subprocess.CalledProcessError:
                print(f"Could not unzip catalog {filePath}")
                raise
```

```python
def _download_file_vizier(cat, filePath,
    catalogname='catalog.dat'):
    sys.stdout.write(f'\rDownloading file
        {os.path.basename(filePath)} from Vizier ...\r')
    sys.stdout.flush()
    os.makedirs(os.path.dirname(filePath), exist_ok=True)
    ntries = 0
    while ntries < _MAX_NTRIES:
        try:
            with FTP('cdsarc.u-strasbg.fr') as ftp:
                ftp.login()
                ftp.cwd(os.path.join('pub', 'cats', cat))
                with open(filePath, 'wb') as savefile:
                    ftp.retrbinary(f'RETR {catalogname}',
                        savefile.write)
            break
        except Exception as e:
            print(f"Attempt {ntries+1}: Failed to download
                {catalogname} - {e}")
            ntries += 1
    if ntries >= _MAX_NTRIES:
        raise IOError(f"File {catalogname} does not exist on
            the server.")

def download_sparc():
    tPath = os.path.join(_CACHE_VIZIER_DIR, 'cats',
        *_LELLI_VIZIER_NAME.split('/'))
    filePath = os.path.join(tPath, 'table2.dat')
    readmePath = os.path.join(tPath, 'ReadMe')
    if not os.path.exists(filePath):
        vizier(_LELLI_VIZIER_NAME, filePath, readmePath,
            catalogname='table2.dat', readmename='ReadMe')
    table = ascii.read(filePath, readme=readmePath,
        format='cds')
    return table.to_pandas()

def read_sparc_data(galaxy):
    raw = download_sparc()
    data = raw[raw['Name'] == galaxy]
    if data.empty:
        raise ValueError(f"Data for the galaxy {galaxy}
            haven't been found!")
    valid = (data['SBdisk'] > 1e-5) & (data['Rad'] > 0)
    data = data[valid]
    if len(data) == 0:
        raise ValueError(f"After filtration, the data for
            {galaxy} are empty!")
    return data
```

```
69
70  def sb_to_mag(sb):
71      return 24.812 - 2.5 * np.log10(sb)
72
73  def plot_sparc_lumprofile(galaxy):
74      data = read_sparc_data(galaxy)
75      mu = sb_to_mag(data['SBdisk'])
76      plt.plot(data['Rad'], mu, marker='o', ls='none',
77          color='k', zorder=1)
77      plt.xlim(0., 1.1 * np.amax(data['Rad']))
78      plt.ylim(np.amax(mu)+1, np.amin(mu)-1)
79      plt.xlabel(r'$R$ [kpc]', fontsize=17)
80      plt.ylabel(r'$\mu$ [mag/arcsec$^{2}$]', fontsize=17)
81
82
83  def model_lumprofile(galaxy):
84      data = read_sparc_data(galaxy)
85      data = data[data['SBdisk'] > 0]
86      ip = interpolate.InterpolatedUnivariateSpline(data['Rad'],
87          np.log(data['SBdisk']), k=3)
87      def lum(R):
88          R = np.atleast_1d(R)
89          out = np.zeros(R.shape)
90          oindx = (R >= np.amin(data['Rad'])) * (R <=
91              np.amax(data['Rad']))
91          out[oindx] = np.exp(ip(R[oindx]))
92          return out * u.Lsun / u.pc**2
93      return lum
94
95  def model_diskpot(MoverL, lumprofile):
96      return AnyAxisymmetricRazorThinDiskPotential(lambda R:
97          MoverL * lumprofile((R/u.kpc).to_value
98          (u.dimensionless_unscaled)), ro=8., vo=220.)
97
98
99  def save_sparc_plots_with_model(galaxy, MoverL):
100
101     plt.figure(figsize=(6, 4))
102     plot_sparc_lumprofile(galaxy)
103     plt.tick_params(axis='both', labelsize=17)
104     plt.title(f"NGC 2998", fontsize=17)
105     plt.tight_layout()
106     plt.savefig(f"{galaxy}_lum.png", dpi=150,
107         bbox_inches='tight')
107     plt.close()
108
109     data = read_sparc_data(galaxy)
110     lumprofile = model_lumprofile(galaxy)
```

```
111      diskpot = model_diskpot(MoverL, lumprofile)

112
113      plt.figure(figsize=(6, 4))

114
115      plt.errorbar(data['Rad'], data['Vobs'],
             yerr=data['e_Vobs'],
116                  marker='o', ls='none', color='k',
                       label='Measured data')

117
118
119      Rs = np.linspace(0.1, 1.1 * np.amax(data['Rad']), 101)
120      vcirc = [diskpot.vcirc(R * u.kpc, use_physical=True) for R
             in Rs]
121      plt.plot(Rs, vcirc, color='darkcyan', lw=2, label=f'model
             (M/L = {MoverL:.2f})')

122
123      plt.xlabel(r'$R$ [kpc]', fontsize=17)
124      plt.ylabel(r'$v_c$ [km/s]', fontsize=17)
125      plt.xlim(0., 1.1 * np.amax(data['Rad']))
126      plt.ylim(0., 1.3 * np.amax(data['Vobs']))
127      plt.tick_params(axis='both', labelsize=17)
128      plt.title(f"NGC 2998", fontsize=17)
129      plt.tight_layout()
130      plt.savefig(f"{galaxy}_rot_model.png",dpi=150,
             bbox_inches='tight')
131      plt.close()

132
133
134  save_sparc_plots_with_model('NGC2998', 0.39 * u.Msun / u.Lsun)
```

Listing 1: *Python code for displaying the luminosity profile and rotation curve with a model (for the galaxy NGC 2998).*

```python
import numpy as np
import matplotlib
matplotlib.use('Agg')
import matplotlib.pyplot as plt
from scipy.optimize import curve_fit
from galpy.potential import NFWPotential, evaluateDensities,
    PseudoIsothermalPotential, HernquistPotential


R0 = 8.0
V0 = 220.0
PC_TO_M = 3.0857e16
MSUN_TO_KG = 1.989e30
DENSITY_CONVERSION = MSUN_TO_KG / (PC_TO_M ** 3)

def vcirc_nfw(r_kpc, amp, a_kpc):
    pot = NFWPotential(amp=amp, a=a_kpc / R0, ro=R0, vo=V0)
    r_galpy = r_kpc / R0
    return np.array([pot.vcirc(R) for R in r_galpy])

def vcirc_iso(r_kpc, amp, a_kpc):
    pot = PseudoIsothermalPotential(amp=amp, a=a_kpc / R0,
        ro=R0, vo=V0)
    r_galpy = r_kpc / R0
    return np.array([pot.vcirc(R) for R in r_galpy])

def vcirc_hernquist(r_kpc, amp, a_kpc):
    pot = HernquistPotential(amp=amp, a=a_kpc / R0, ro=R0,
        vo=V0)
    r_galpy = r_kpc / R0
    return np.array([pot.vcirc(R) for R in r_galpy])



def fit_velocity_curve(filename):
    data = np.loadtxt(filename, skiprows=7)
    r_kpc = data[:, 0]
    v_kms = data[:, 3]


    p0_nfw = [1.0, 5.0]
    p0_iso = [1.0, 5.0]
    p0_hern = [1.0, 5.0]


    bounds_nfw = ([0.01, 0.1], [500, 1000])
```

```
45    bounds_iso = ([0.001, 0.001], [100, 100])
46    bounds_hern = ([0.01, 0.1], [900, 100])
47
48
49    popt_nfw, _ = curve_fit(vcirc_nfw, r_kpc, v_kms,
          p0=p0_nfw, bounds=bounds_nfw)
50    popt_iso, _ = curve_fit(vcirc_iso, r_kpc, v_kms,
          p0=p0_iso, bounds=bounds_iso)
51    popt_hern, _ = curve_fit(vcirc_hernquist, r_kpc, v_kms,
          p0=p0_hern, bounds=bounds_hern)
52
53
54    r_eval = np.linspace(min(r_kpc), max(r_kpc), 500)
55    v_nfw = vcirc_nfw(r_eval, *popt_nfw)
56    v_iso = vcirc_iso(r_eval, *popt_iso)
57    v_hern = vcirc_hernquist(r_eval, *popt_hern)
58
59
60    plt.figure()
61    plt.plot(r_kpc, v_kms, color='black', linewidth=3,
          label=r'$v_{\text{DM}}$')
62    plt.plot(r_eval, v_nfw, linestyle='dashed',
          color='lightseagreen', label='NFW')
63    plt.plot(r_eval, v_iso, linestyle='dashed',
          color='orange', label='pISO')
64    plt.plot(r_eval, v_hern, linestyle='dashed',
          color='darkorchid', label='Hernquist')
65    plt.xlabel(r'$r$ [kpc]', fontsize=17)
66    plt.xlim(0,50)
67    plt.ylabel(r'$v_{\text{DM}}$ [km/s]', fontsize=17)
68    plt.legend()
69    plt.tick_params(axis='both', labelsize=17)
70    plt.legend(fontsize=14, loc='lower right')
71    plt.title('NGC 2998', fontsize=17)
72    plt.savefig('ngc2998_dm_velocity_curve_fit.png', dpi=150,
          bbox_inches='tight')
73
74    print("Fitted NFW parameters: amp = {:.3f}, a =
          {:.3f}".format(*popt_nfw))
75    print("Fitted Hernquist parameters: amp = {:.3f}, a =
          {:.3f}".format(*popt_hern))
76    print("Fitted Pseudo-Isothermal parameters: amp = {:.3f},
          a = {:.3f}".format(*popt_iso))
77
78    return popt_nfw, popt_iso, popt_hern
79
80
81
```

```python
def plot_nfw_density_profile(amp, a,
    filename='ngc2998_nfw_density_profile_kg_m3.png'):
    pot = NFWPotential(amp=amp, a=a, ro=RO, vo=VO)
    r_kpc = np.linspace(0.1, 50, 200)
    R_vals = r_kpc / RO
    z = 0.0
    densities_kpc = [evaluateDensities(pot, R, z,
        use_physical=True) for R in R_vals]
    densities_si = [d * DENSITY_CONVERSION for d in
        densities_kpc]

    plt.figure()
    plt.plot(r_kpc, densities_si, color='teal')
    plt.xlabel('$r$ [kpc]', fontsize=17)
    plt.ylabel(r'$\rho_{\text{DM}}$ [kg/m$^3$]', fontsize=17)
    plt.xlim(0,50)
    plt.yscale('log')
    plt.title('NGC 2998, NFW', fontsize=17)
    plt.tick_params(axis='both', labelsize=17)
    plt.savefig(filename, dpi=150, bbox_inches='tight')
    print(f"Saved density profile to '{filename}'")

    save_data = np.vstack([r_kpc, densities_si]).T
    np.savetxt(f"{filename}.txt", save_data, fmt='%.6e',
        header='r_kpc    rho_kg_per_m3')



def plot_iso_density_profile_kg_m3(amp, a,
    filename='ngc2998_iso_density_profile_kg_m3.png'):
    pot = PseudoIsothermalPotential(amp=amp, a=a, ro=RO, vo=VO)
    r_kpc = np.linspace(0.1, 50, 200)
    R_vals = r_kpc / RO
    z = 0.0
    densities_pc = [evaluateDensities(pot, R, z,
        use_physical=True) for R in R_vals]
    densities_si = [d * DENSITY_CONVERSION for d in
        densities_pc]

    plt.figure()
    plt.plot(r_kpc, densities_si, color='teal')
    plt.xlabel('$r$ [kpc]', fontsize=17)
    plt.ylabel(r'$\rho_{\text{DM}}$ [kg/m$^3$]', fontsize=17)
    plt.xlim(0,50)
    plt.yscale('log')
    plt.title('NGC 2998, pISO', fontsize=17)
    plt.tick_params(axis='both', labelsize=17)
    plt.savefig(filename, dpi=150, bbox_inches='tight')
```

```python
print(f"Saved ISO density profile to '{filename}'")

save_data = np.vstack([r_kpc, densities_si]).T
np.savetxt(f"{filename}.txt", save_data, fmt='%.6e',
    header='r_kpc      rho_kg_per_m3')


def plot_hern_density_profile_kg_m3(amp, a,
    filename='ngc2998_hern_density_profile_kg_m3.png'):
    pot = HernquistPotential(amp=amp, a=a, ro=RO, vo=VO)
    r_kpc = np.linspace(0.1, 50, 200)
    R_vals = r_kpc / RO
    z = 0.0
    densities_kpc = [evaluateDensities(pot, R, z,
        use_physical=True) for R in R_vals]
    densities_si = [d * DENSITY_CONVERSION for d in
        densities_kpc]

    plt.figure()
    plt.plot(r_kpc, densities_si, color='teal')
    plt.xlabel('$r$ [kpc]', fontsize=17)
    plt.ylabel(r'$\rho_{\text{DM}}$ [kg/m$^3$]', fontsize=17)
    plt.xlim(0,50)
    plt.yscale('log')
    plt.title('NGC 2998, Hernquist', fontsize=17)
    plt.tick_params(axis='both', labelsize=17)
    plt.savefig(filename, dpi=150, bbox_inches='tight')
    print(f"Saved Hernquist density profile to '{filename}'")

    save_data = np.vstack([r_kpc, densities_si]).T
    np.savetxt(f"{filename}.txt", save_data, fmt='%.6e',
        header='r_kpc      rho_kg_per_m3')


popt_nfw, popt_iso, popt_hern =
    fit_velocity_curve('NGC2998_rotcurve_components.txt')


plot_nfw_density_profile(*popt_nfw)
plot_iso_density_profile_kg_m3(*popt_iso)
plot_hern_density_profile_kg_m3(*popt_hern)
```

Listing 2: *Python code for fitting the NFW, pseudo-isothermal and Hernquist models to the v_{DM} curve and for plotting the dark matter density with the obtained parameters for each model (for the galaxy NGC 2998).*

B   Data Tables

Table 8: *NGC 2998 (SPARC data)*

r (kpc)	V_{obs} (km/s)	$e_{V_{\mathrm{obs}}}$ (km/s)	μ_{disk} ($L_{\odot}/\mathrm{pc}^2$)
0.33	90.00	20.00	2070.29
0.99	125.00	15.00	1190.44
1.98	148.00	15.00	888.44
2.64	180.00	17.00	784.11
3.63	201.00	15.00	702.55
7.59	206.00	10.00	192.87
12.50	214.00	5.00	56.10
17.48	212.00	5.00	17.41
22.46	213.00	2.00	10.54
27.44	214.00	2.00	5.26
32.32	213.00	2.00	2.50
37.30	213.00	3.00	0.96
42.28	203.00	3.00	0.33

Table 9: *NGC 2366 (SPARC data)*

r (kpc)	V_{obs} (km/s)	$e_{V_{\text{obs}}}$ (km/s)	μ_{disk} (L$_\odot$/pc^2)
0.12	4.20	3.15	51.70
0.36	9.41	1.83	47.22
0.59	15.30	1.37	35.13
0.83	18.40	1.64	28.17
1.07	23.40	2.08	17.57
1.31	28.10	2.46	11.56
1.54	33.10	2.01	7.62
1.79	37.50	1.62	5.72
2.02	40.50	1.68	4.38
2.26	42.30	1.69	2.95
2.49	45.20	1.91	1.90
2.74	47.40	1.95	1.32
2.97	48.10	1.74	0.93
3.21	48.80	1.08	0.64
3.44	50.70	1.55	0.45
3.69	52.10	2.78	0.31
3.92	53.00	2.98	0.22
4.16	53.70	2.39	0.15
4.40	51.20	2.21	0.10
4.64	51.60	1.45	0.07
4.87	51.50	1.84	0.05
5.11	50.40	2.53	0.03
5.35	48.50	4.60	0.02
5.59	50.00	5.91	0.02
5.82	49.00	7.42	0.01
6.06	49.40	5.92	0.00

Table 10: *NGC 1705 (SPARC data)*

r (kpc)	V_{obs} (km/s)	$e_{V_{obs}}$ (km/s)	μ_{disk} ($L_\odot/pc^2$)
0.22	50.20	7.50	512.85
0.66	62.20	7.51	84.05
1.11	72.40	5.35	25.33
1.55	73.20	3.31	8.23
2.00	72.90	3.21	3.00
2.45	72.60	2.73	0.83
2.89	71.50	3.41	0.29
3.34	71.10	4.38	0.09
3.78	71.40	4.60	0.03
4.22	71.50	5.68	0.01
4.66	71.50	6.20	0.00
5.11	71.30	6.43	0.00
5.56	71.80	9.68	0.00
6.00	71.50	10.50	0.00

Table 11: *NGC 5371 (SPARC data)*

r (kpc)	V_{obs} (km/s)	$e_{V_{obs}}$ (km/s)	μ_{disk} ($L_\odot/pc^2$)
1.45	216.00	10.00	1579.45
2.88	215.00	7.00	725.11
4.33	215.00	5.00	586.66
5.78	214.00	4.00	431.16
7.22	215.00	4.00	356.04
8.66	221.00	3.00	328.20
11.55	233.00	3.00	253.05
14.48	237.00	3.00	153.39
17.28	242.00	3.00	98.50
20.20	241.00	3.00	65.35
23.12	240.00	3.00	32.44
26.04	234.00	3.00	13.89
28.84	226.00	3.00	7.22
31.76	213.00	3.00	4.16
34.68	207.00	3.00	1.44
37.48	208.00	4.00	0.00
40.40	209.00	4.00	0.00
43.32	207.00	4.00	0.00
46.24	213.00	6.00	0.00

Table 12: *NGC 3198 (SPARC data)*

r (kpc)	V_{obs} (km/s)	$e_{V_{\mathrm{obs}}}$ (km/s)	μ_{disk} (L$_\odot$/pc^2)
0.32	24.40	35.90	1084.92
0.64	43.30	16.30	590.57
0.96	45.50	16.10	410.97
1.28	58.50	15.40	329.34
1.61	68.80	7.61	268.62
1.93	76.90	10.30	247.67
2.24	82.00	8.09	227.56
2.57	86.90	7.60	205.02
2.89	97.60	3.03	200.20
3.21	100.00	5.31	208.58
3.54	107.00	7.51	208.47
3.85	113.00	7.32	196.07
4.17	117.00	5.21	179.96
4.50	119.00	5.67	164.19
4.82	127.00	5.39	150.99
5.15	132.00	4.34	138.08
5.46	134.00	2.36	126.00
5.78	137.00	0.89	113.63
6.10	140.00	2.84	101.19
6.43	142.00	0.88	86.52
6.74	144.00	1.23	70.23
7.06	146.00	1.57	57.67
8.04	147.00	3.00	40.74
9.04	148.00	3.00	31.83
10.04	152.00	2.00	26.64
11.04	155.00	2.00	21.02
12.05	156.00	2.00	15.42
14.05	157.00	2.00	6.42
16.07	153.00	2.00	2.95
18.13	153.00	2.00	2.39
20.05	154.00	2.00	1.44
22.12	153.00	2.00	0.72
24.03	150.00	2.00	0.28
26.10	149.00	2.00	0.16
28.16	148.00	2.00	0.08
30.08	146.00	2.00	0.04
32.14	147.00	2.00	0.02
34.06	148.00	2.00	0.01
36.12	148.00	2.00	0.01
38.19	149.00	2.00	0.00
40.10	150.00	2.00	0.00
42.17	150.00	3.00	0.00
44.08	149.00	3.00	0.00

Table 13: *NGC 2903 (SPARC data)*

r (kpc)	V_{obs} (km/s)	$e_{V_{obs}}$ (km/s)	μ_{disk} (L$_\odot$/pc^2)
0.32	44.00	8.00	7393.57
0.64	64.00	8.00	3002.08
0.96	128.00	8.00	2411.81
1.28	148.00	8.00	1895.47
1.60	157.00	8.00	1625.63
1.92	189.00	8.00	1474.21
2.24	195.00	6.00	1493.06
2.56	201.00	6.00	1371.30
2.88	214.00	4.00	1009.96
3.20	215.00	4.00	706.79
3.52	215.00	4.00	476.79
3.84	216.00	3.00	365.53
4.80	214.00	2.00	195.17
5.76	210.00	2.00	83.13
6.72	205.00	2.00	50.66
7.68	203.00	1.00	32.24
8.64	201.00	1.00	23.57
9.60	201.00	1.00	14.07
10.56	199.00	1.00	10.06
11.52	197.00	1.00	6.57
12.48	196.00	2.00	4.46
13.44	193.00	3.00	2.89
14.40	190.00	3.00	1.89
15.36	188.00	5.00	1.25
16.32	187.00	5.00	0.83
17.28	188.00	3.00	0.55
18.24	186.00	3.00	0.37
19.20	185.00	3.00	0.24
20.16	185.00	3.00	0.16
21.12	181.00	3.00	0.11
22.08	178.00	3.00	0.07
23.04	177.00	3.00	0.05
24.00	182.00	4.00	0.03
24.96	180.00	8.00	0.00

References

Aprile, E. and Others (2019). Constraining the spin-dependent wimp-nucleon cross sections with xenon1t. *Physical Review Letters*, 122(14).

Begeman, K. G., Broeils, A. H., and Sanders, R. H. (1991). Extended rotation curves of spiral galaxies : dark haloes and modified dynamics. *Monthly Notices of the Royal Astronomical Society*, 249:523.

Binney, J. and Tremaine, S. (1987). *Galactic dynamics*.

Bovy, J. (2015). galpy: A python LIBRARY FOR GALACTIC DYNAMICS. *The Astrophysical Journal Supplement Series*, 216(2):29.

Bovy, J. (2023). Dynamics and astrophysics of galaxies. *Princeton University Press,Princeton, NJ (in preparation)*.

Bovy, J. and Tremaine, S. (2012). On the local dark matter density. *The Astrophysical Journal*, 756(1):89.

Bradley, L., Sipőcz, B., Robitaille, T., Tollerud, E., Vinícius, Z., Deil, C., Barbary, K., Wilson, T. J., Busko, I., Donath, A., Günther, H. M., Cara, M., Lim, P. L., Meßlinger, S., Conseil, S., Burnett, Z., Bostroem, A., Droettboom, M., Bray, E. M., Bratholm, L. A., Ginsburg, A., Jamieson, W., Barentsen, G., Craig, M., Morris, B. M., Perrin, M., Rathi, S., Pascual, S., and Georgiev, I. Y. (2024). astropy/photutils: 2.0.2.

Ciccolella, A. and De Leo, M. (2016). Hubble - de Vaucouleurs diagram for galaxy morphology featuring ellipticals, lenticulars, spirals, intermediate spirals, barred spirals and irregulars.

Clausius, R. (1870). Ueber einen auf die Wärme anwendbaren mechanischen Satz. *Annalen der Physik*, 217(9):124–130.

Combes, F. (2023). Spiral galaxies.

de Vaucouleurs, G. (1948). Recherches sur les Nebuleuses Extragalactiques. *Annales d'Astrophysique*, 11:247.

de Vaucouleurs, G. (1963). Revised Classification of 1500 Bright Galaxies. *The Astrophysical Journal Supplement Series*, 8:31.

Dehnen, W., McLaughlin, D. E., and Sachania, J. (2006). The velocity dispersion and mass profile of the milky way: Velocity dispersion profile of the milky way. *Monthly Notices of the Royal Astronomical Society*, 369(4):1688–1692.

DES Collaboration, Abbott, T. M. C., and Others (2025). Dark energy survey: implications for cosmological expansion models from the final des baryon acoustic oscillation and supernova data.

Dodelson, S., Gates, E. I., and Turner, M. S. (1996). Cold Dark Matter. *Science*, 274(5284):69–75.

ESA, NASA, and Massey, R. (2007). 3D map of dark matter as seen by Hubble.

ESA/Euclid/Euclid Consortium/NASA, Walmsley, M., Huertas, M., and Cuillandre, J., C. (2025). Galaxies in different shapes captured by Euclid.

ESA/Webb, NASA & CSA, and Mahler, G. (2025). Spying a spiral through a cosmic lens.

Euclid Consortium (2025a). Euclid consortium: New science results and exclusive data from the euclid space telescope.

Euclid Consortium (2025b). Euclid Consortium a space mission to map the dark universe.

Faber, S. M. and Jackson, R. E. (1976). Velocity dispersions and mass-to-light ratios for elliptical galaxies. *The Astrophysical Journal*, 204:668–683.

Freese, K. (2017). Status of dark matter in the universe. *International Journal of Modern Physics D*, 26(06):1730012.

Garcon, A., Aybas, D., Blanchard, J. W., Centers, G., Figueroa, N. L., Graham, P. W., Kimball, D. F. J., Rajendran, S., Sendra, M. G., Sushkov, A. O., Trahms, L., Wang, T., Wickenbrock, A., Wu, T., and Budker, D. (2017). The cosmic axion spin precession experiment (casper): a dark-matter search with nuclear magnetic resonance. *Quantum Science and Technology*, 3(1):014008.

Hernquist, L. (1990). An Analytical Model for Spherical Galaxies and Bulges. *The Astrophysical Journal*, 356:359.

Hubble, E. (1936). *THE REALM OF THE NEBULAE.*

Kamionkowski, M. (1998). The Case of the Curved Universe: Open, Closed, or Flat? *Science*, 280:1397.

Khatiwada, R., Bowring, D., Chou, A. S., Sonnenschein, A., Wester, W., Mitchell, D. V., Braine, T., Bartram, C., Cervantes, R., Crisosto, N., Du, N., Rosenberg, L. J., Rybka, G., Yang, J., Will, D., Kimes, S., Carosi, G., Woollett, N., Durham, S., Duffy, L. D., Bradley, R., Boutan, C., Jones, M., LaRoque, B. H., Oblath, N. S., Taubman, M. S., Tedeschi, J., Clarke, J., Dove, A., Hashim, A., Siddiqi, I., Stevenson, N., Eddins, A., O'Kelley, S. R., Nawaz, S., Agrawal, A., Dixit, A. V., Gleason, J. R., Jois, S., Sikivie, P., Sullivan, N. S., Tanner, D. B., Solomon, J. A., Lentz, E., Daw, E. J., Perry, M. G., Buckley, J. H., Harrington, P. M., Henriksen, E. A., Murch, K. W., and Hilton, G. C. (2021). Axion dark matter experiment: Detailed design and operations. *Review of Scientific Instruments*, 92(12).

Kormendy, J. and Kennicutt, Jr., R. C. (2004). Secular Evolution and the Formation of Pseudobulges in Disk Galaxies. *Annual Review of Astronomy and Astrophysics*, 42(1):603–683.

Kowalczyk, K., Łokas, E. L., and Valluri, M. (2017). Recovering the mass profile and orbit anisotropy of mock dwarf galaxies with schwarzschild modelling. *Monthly Notices of the Royal Astronomical Society*, 470(4):3959–3969.

Kravtsov, A. V. (2013). The Size-Virial Radius Relation of Galaxies. *The Astrophysical Journal Letters*, 764(2):L31.

Kurfürst, P., Zajaček, M., Werner, N., and Krtička, J. (2024). Red giant - jet collisions in galactic nuclei I: 3D hydrodynamical model of a few stellar orbits. *arXiv e-prints*, page arXiv:2409.17773.

Kurfürst, P. (2024). Models of hot star decretion disks.

Lahav, O. and Liddle, A. R. (2004). The Cosmological Parameters. *arXiv e-prints*, pages astro–ph/0406681.

Lelli, F., McGaugh, S. S., and Schombert, J. M. (2016). SPARC: Mass Models for 175 Disk Galaxies with Spitzer Photometry and Accurate Rotation Curves. *The Astronomical Journal*, 152(6):157.

Leo, M. D. (2018). Rotation curve of spiral galaxy Messier 33.

Li, P., Lelli, F., McGaugh, S., and Schombert, J. (2020). A Comprehensive Catalog of Dark Matter Halo Models for SPARC Galaxies. *The Astrophysical Journal Supplement Series*, 247(1):31.

Li, X., Tang, L., and Lin, H.-N. (2017). Comparing dark matter models, modified newtonian dynamics and modified gravity in accounting for galaxy rotation curves. *Chinese Physics C*, 41(5):055101.

McGaugh, S. S., Schombert, J. M., Bothun, G. D., and de Blok, W. J. G. (2000). The Baryonic Tully-Fisher Relation. *The Astrophysical Journal Letters*, 533(2):L99–L102.

Mikulášek, Z. and Krtička, J. (2005). *Základy fyziky hvězd*.

Milgrom, M. (1983a). A modification of the Newtonian dynamics - Implications for galaxies. *The Astrophysical Journal*, 270:371–383.

Milgrom, M. (1983b). A modification of the Newtonian dynamics as a possible alternative to the hidden mass hypothesis. *The Astrophysical Journal*, 270:365–370.

Miyamoto, M. and Nagai, R. (1975). Three-dimensional models for the distribution of mass in galaxies. *Publications of the Astronomical Society of Japan*, 27:533–543.

Moorthy, B. K. and Holtzman, J. A. (2006). Stellar populations in bulges of spiral galaxies. *Monthly Notices of the Royal Astronomical Society*, 371(2):583–608.

Mortlock, D. J. and Turner, E. L. (2001). Gravitational lensing in modified Newtonian dynamics. *Monthly Notices of the Royal Astronomical Society*, 327(2):557–566.

NASA, JPL-Caltech, and ESA (2013). PIA16874: The Universe Comes into Sharper Focus.

NASA and WMAP Science Team (2011). Geometry of the Universe.

NASA/CXC/CfA/M. Markevitch, NASA/STScI, Magellan/U.Arizona/D. Clowe, and ESO WFI (2007). The Bullet Cluster. X-ray: NASA/CXC/CfA/M. Markevitch, Optical and lensing map: NASA/STScI, Magellan/U.Arizona/D. Clowe, Lensing map: ESO WFI.

NASA/ESA/M.J. Jee (2007). Galaxy Cluster Cl 0024+17.

Navarro, J. F., Frenk, C. S., and White, S. D. M. (1996). The Structure of Cold Dark Matter Halos. *The Astrophysical Journal*, 462:563.

Oh, S.-H., de Blok, W. J. G., Walter, F., Brinks, E., and Kennicutt, Jr., R. C. (2008). High-Resolution Dark Matter Density Profiles of THINGS Dwarf Galaxies: Correcting for Noncircular Motions. *The Astronomical Journal*, 136(6):2761–2781.

Pfrommer, C. (2022). *Theoretical Astrophysics with Applications to Galaxies and Galaxy Clusters*.

Planck Collaboration and Others (2016). Planck 2015 results: Xiii. cosmological parameters. *Astronomy & Astrophysics*, 594:A13.

Rubin, V. C., Ford, Jr., W. K., and Thonnard, N. (1978). Extended rotation curves of high-luminosity spiral galaxies. IV. Systematic dynamical properties, Sa -> Sc. *The Astrophysical Journal*, 225:L107–L111.

Rubin, V. C., Ford, Jr., W. K., and Thonnard, N. (1980). Rotational properties of 21 SC galaxies with a large range of luminosities and radii, from NGC 4605 (R=4kpc) to UGC 2885 (R=122kpc). *The Astrophysical Journal*, 238:471–487.

Said, K. (2023). Tully-fisher relation.

Salucci, P. (2019). The distribution of dark matter in galaxies. *The Astronomy and Astrophysics Review*, 27(1).

Sersic, J. L. (1968). *Atlas de Galaxias Australes*.

Sofue, Y. and Rubin, V. (2001). Rotation Curves of Spiral Galaxies. *Annual Review of Astronomy and Astrophysics*, 39:137–174.

Springel, V. and Others (2020). The Cosmic Web (Artist's Impression) a space mission to map the dark universe.

Springel, V., Yoshida, N., and White, S. D. M. (2001). GADGET: a code for collisionless and gasdynamical cosmological simulations. *New Astronomy*, 6(2):79–117.

Tully, R. B. and Fisher, J. R. (1977). A new method of determining distances to galaxies. *Astronomy & Astrophysics*, 54:661–673.

van Albada, T. S., Bahcall, J. N., Begeman, K., and Sancisi, R. (1985). Distribution of dark matter in the spiral galaxy NGC 3198. *The Astrophysical Journal*, 295:305–313.

van den Bergh, S. (1960a). A Preliminary Luminosity Classification for Galaxies of Type Sb. *The Astrophysical Journal*, 131:558.

van den Bergh, S. (1960b). A Preliminary Luminosity Clssification of Late-Type Galaxies. *The Astrophysical Journal*, 131:215.

van den Bergh, S. (1960c). A reclassification of the northern Shapley-Ames galaxies. *Publications of the David Dunlap Observatory*, 2(6):159–199.

Wechsler, R. H. and Tinker, J. L. (2018). The Connection Between Galaxies and Their Dark Matter Halos. *Annual Review of Astronomy and Astrophysics*, 56:435–487.

XENON Collaboration and Others (2024). The xenonnt dark matter experiment.

Zejda, M. (2013). Základy astronomie.